

AD-A086 213

BOEING AEROSPACE CO SEATTLE WA  
DIFFRACTION PHASE LOADING OF STRUCTURES. (U)  
OCT 78 J ETZWILER

F/O 1/3

UNCLASSIFIED

DNA-4726F

DNA001-78-C-0138

NL

1 OF 1  
AD-A086 213

END  
DATE  
FILMED  
8-80  
DTIC

ADA 086213

12 LEVEL II

AD-E 300 818

DNA 4726F

# DIFFRACTION PHASE LOADING OF STRUCTURES

Boeing Aerospace Company  
P.O. Box 3999  
Seattle, Washington 98124

31 October 1978

Final Report for Period 24 January 1978-31 October 1978

CONTRACT No. DNA 001-78-C-0138

APPROVED FOR PUBLIC RELEASE;  
DISTRIBUTION UNLIMITED.

THIS WORK SPONSORED BY THE DEFENSE NUCLEAR AGENCY  
UNDER RDT&E RMSS CODE B342078464 N99QAXAK50602 H2590D.

Prepared for  
Director  
DEFENSE NUCLEAR AGENCY  
Washington, D. C. 20305

DTIC  
ELECTE  
S JUL 8 1980 D  
B

80 5 14 067

DDC FILE COPY

Destroy this report when it is no longer needed. Do not return to sender.

PLEASE NOTIFY THE DEFENSE NUCLEAR AGENCY,  
ATTN: STTI, WASHINGTON, D.C. 20305, IF  
YOUR ADDRESS IS INCORRECT, IF YOU WISH TO  
BE DELETED FROM THE DISTRIBUTION LIST, OR  
IF THE ADDRESSEE IS NO LONGER EMPLOYED BY  
YOUR ORGANIZATION.



UNCLASSIFIED

SECURITY CLASSIFICATION OF THIS PAGE (When Data Entered)

REPORT DOCUMENTATION PAGE		READ INSTRUCTIONS BEFORE COMPLETING FORM
1. REPORT NUMBER DNA 4/26F	2. GOVT ACCESSION NO. AD-A086213	3. RECIPIENT'S CATALOG NUMBER
4. TITLE (and Subtitle) 6. DIFFRACTION PHASE LOADING OF STRUCTURES.	7. AUTHOR(s) 10. J. Etwiler	5. TYPE OF REPORT & PERIOD COVERED 9. Final Report, for Period 24 Jan 78 - 31 Oct 78
9. PERFORMING ORGANIZATION NAME AND ADDRESS Boeing Aerospace Company ✓ P.O. Box 3999 Seattle, Washington 98124	11. CONTROLLING OFFICE NAME AND ADDRESS Director Defense Nuclear Agency Washington, D.C. 20305	8. CONTRACT OR GRANT NUMBER(s) DNA 001-78-C-0138 ✓
14. MONITORING AGENCY NAME & ADDRESS (if different from Controlling Office)	12. REPORT DATE 11. 31 October 1978	10. PROGRAM ELEMENT PROJECT, TASK AREA & WORK UNIT NUMBERS 16. Subtask N99QAXAK506-02
16. DISTRIBUTION STATEMENT (of this Report) 12. 86 Approved for public release; distribution unlimited.	13. NUMBER OF PAGES 86	15. SECURITY CLASS (of this report) UNCLASSIFIED
17. DISTRIBUTION STATEMENT (of the abstract entered in block 20, if different from Report) 17. K506	15a. DECLASSIFICATION DOWNGRADING SCHEDULE	
18. DNA SBIE	19. 4726F AD-E300 818	
18. SUPPLEMENTARY NOTES This work sponsored by the Defense Nuclear Agency under RDT&E RMSS Code B342078464 N99QAXAK50602 H2590D.		
19. KEY WORDS (Continue on reverse side if necessary and identify by block number) VIBRA-4                      Diffraction Nuclear                        Structure Gust		
20. ABSTRACT (Continue on reverse side if necessary and identify by block number) The response of the KC-135 and 747 aircraft to a nuclear gust were calculated using the VIBRA-4 code. Runs were made with and without diffraction phase loading to determine the effect on the aircraft response. The differences in the calculated ratios were small for the KC-135 model, but large differences were found with the 747 model. Clearly the diffraction phase can exert a large influence on the nuclear gust imposed loads, but it was not possible to predict this effect in advance.		

059610

SW

PREFACE

This work was funded by the Defense Nuclear Agency under contract DNA001-78-C-0138 as a continuing part of a study of mission completion of strategic aircraft. Capt. M. Rafferty was the Contracting Officer's Representative and we gratefully acknowledge his support and helpful comments.

The work was performed by Mr. J. Etzweiler as Technical Leader, and Dr. S. L. Strack as the Program Manager.

ACCESSION for		
NTIS	White Section	<input checked="" type="checkbox"/>
DDC	Buff Section	<input type="checkbox"/>
UNANNOUNCED		<input type="checkbox"/>
JUSTIFICATION		
BY		
DISTRIBUTION/AVAILABILITY CODES		
Dist.	AVAIL. and/or	SPECIAL
A		-

## SUMMARY

The response of KC-135 and 747 type aircraft to a nuclear burst was calculated using the VIBRA-4 code. Runs were made with and without the diffraction phase loading to determine its effect on the aircraft response.

Bending moments were computed for stations on the fuselage, wing, horizontal and vertical stabilizers, for bursts from below, above, and to the side. The ratios of peak bending moments, with and without the diffraction phase were calculated. The differences in the calculated ratios were small for the KC-135 model, but large differences were found for the 747 models. It is clear that the diffraction phase loads can exert a large influence on the nuclear gust imposed loads, but it is not possible to predict this effect with any confidence in advance of detailed calculations.

Thus any computer codes for nuclear gust response should include the diffraction phase loads. Further work should be made to verify loading trends identified in this study.

CONVERSION FACTORS FOR U.S. CUSTOMARY  
TO METRIC (SI) UNITS OF MEASUREMENT

To Convert From	To	Multiply By
foot	meter (m)	3.048 000 X E -1
foot/second (fps)	meter per second (m/s)	3.048 000 X E -1
inch	meter (m)	2.540 000 X E -2
kilotons	terajoules	4.183
kip (1000 lbf)	newton (N)	4.448 222 X E +3
kip/inch <sup>2</sup> (ksi)	kilo pascal (kPa)	6.894 757 X E +3
knots	meter per second (m/s)	5.144 444 X E -1
nautical miles	meters (m)	1.852 000 X E +3
pound-force (lbf avoirdupois)	newton (N)	4.448 222
pound-force inch	newton-meter (N m)	1.129 848 X E -1
pound-force/inch <sup>2</sup> (psi)	kilo pascal (kPa)	6.894 757
pound-mass (lbm avoirdupois)	kilogram (kg)	4.535 924 X E -1
pound-mass-foot <sup>2</sup> (moment of inertia)	kilogram-meter <sup>2</sup> (kg m <sup>2</sup> )	4.214 011 X E -2
pound/square foot (psf)	kilogram per meter <sup>2</sup> (kg/m <sup>2</sup> )	4.882 428
slug	kilogram (kg)	1.459 390 X E +1
square foot (sq. ft., ft <sup>2</sup> )	meter <sup>2</sup> (m <sup>2</sup> )	9.290 304 X E -2

A more complete listing of conversions may be found in "Metric Practice Guide E 380-74," American Society for Testing and Materials.

## TABLE OF CONTENTS

<u>Title</u>	<u>Page</u>
1.0 INTRODUCTION	9
2.0 COMPARISON OF DIFFRACTION PHASE METHODS	11
2.1 DNA 2048H-1	11
2.2 NOVA-2	11
2.3 VIBRA-4	12
2.4 VIBRA-6	12
3.0 GUST ANALYSIS METHODOLOGY	13
3.1 VIBRA-4 Equations of Motion	14
3.1.1 Kinetic Energy	14
3.1.2 Potential Energy	19
3.1.3 Generalized Forces	20
3.1.4 Equation of Motion	20
3.2 Aerodynamic Loading	21
3.3 Gust Environment	24
3.4 Flight Load Allowables	25
4.0 DIFFRACTION PHASE LOADS	28
4.1 Dynamic Model KC-135	28
4.2 Dynamic Model 747-200	32
4.3 Comparison of VIBRA-4 Results	35
5.0 CONCLUSIONS	39
6.0 RECOMMENDATIONS	40
7.0 REFERENCES	41

## LIST OF ILLUSTRATIONS

<u>Figure No.</u>	<u>Title</u>	<u>Page</u>
1	Gust analysis coordinate system	43
2	Two dimensional normal force coefficient	44
3	Fuselage allowable moment boundary	45
4	Overpressure as a function of range	46
5	Normal force coefficient without diffraction phase	47
6	KC-135 right hand wing - blast from below	48
7	KC-135 right hand wing - blast from below	49
8	KC-135 right hand horizontal stabilizer - blast from below	50
9	KC-135 body vertical bending - blast from below	51
10	KC-135 right hand wing - blast from above	52
11	KC-135 right hand wing - blast from above	53
12	KC-135 right hand horizontal stabilizer - blast from above	54
13	KC-135 body vertical bending - blast from above	55
14	KC-135 right hand wing - blast from the side	56
15	KC-135 right hand wing - blast from the side	57
16	KC-135 left hand horizontal stabilizer - blast from the side	58
17	KC-135 vertical body bending - blast from the side	59
18	KC-135 horizontal body bending - blast from the side	60
19	KC-135 fin - blast from the side	61
20	747 right hand wing - blast from below	62
21	747 right hand wing - blast from below	63
22	747 right hand wing - blast from below	64
23	747 right hand wing - blast from below	65
24	747 right hand horizontal stabilizer - blast from below	66
25	747 vertical body bending - blast from below	67
26	747 vertical body bending - blast from below	68
27	747 right hand wing - blast from above	69
28	747 right hand wing - blast from above	70
29	747 right hand wing - blast from above	71

LIST OF ILLUSTRATIONS (Continued)

<u>Figure No.</u>	<u>Title</u>	<u>Page</u>
30	747 right hand horizontal stabilizer - blast from above	72
31	747 vertical body bending - blast from above	73
32	747 vertical body bending - blast from above	74
33	747 right hand wing - blast from side	75
34	747 right hand wing - blast from side	76
35	747 left hand horizontal stabilizer - blast from side	77
36	747 vertical body bending - blast from side	78
37	747 horizontal body bending - blast from side	79
38	747 horizontal body bending - blast from side	80
39	747 fin - blast from side	81

LIST OF TABLES

<u>Table No.</u>	<u>Title</u>	<u>Page</u>
1	KC-135 component bending locations for gust analysis	30
2	KC-135 allowable loads for major components	31
3	747-200 component bending moment locations for gust analysis	33
4	747-200 allowable loads for major components	34
5	KC-135 flight condition	35
6	KC-135 peak bending moment ratio summary	36
7	747-200 flight condition	37
8	747-200 peak bending moment ratio summary	38

## 1.0 INTRODUCTION

In order for our strategic forces to remain a credible deterrent, it is necessary that they have a demonstrated capability to perform their mission. This demonstration has many aspects and one of these is to show by analyses that sufficient weapon systems will survive an attack and be able to complete their mission of inflicting unacceptable damage on the attacker. Policy makers must have high confidence in such analyses for the analyses will reveal the strengths and weaknesses in our various weapon systems. Then the policy makers will guide the development of improvements or change in our defense system. To that end the following study was conducted to evaluate a particular portion of the analytic tools available. This study was concerned with the importance of modeling the aerodynamic forces on an aircraft in the time period immediately after shock arrival.

The aerodynamic forces acting on an airfoil are the result of pressure on the airfoil surfaces. The difference in pressure between upper and lower surfaces of a wing for example results in lift. Pressure depends on the airflow pattern around the airfoil. When the airflow pattern is abruptly changed there is a time of transition until a new airflow pattern and new pressure patterns are established.

A shock wave passing over an airfoil (or any structure) produces unbalanced overpressure forces. Initially only the surface first encountered experiences overpressure, then more and more of the surface experiences overpressure as the shock wave engulfs the structure. At the initial encounter the shock wave is reflected and the front surface experiences the reflected shock overpressure. When the shock wave completely engulfs the structure a rarefaction wave propagates back to the front face of the structure and reduces the reflected shock pressure to its unreflected value. This period is often referred to as the diffraction phase. Aerodynamic loads during the diffraction phase are uncertain for two reasons. First, the proper reflection factors to use for the complex aerodynamic shape of airfoils are not accurately known. Measurements of reflection factors have been made for simple shapes, such as inclined planes and cylinders, but not for complex shapes. Second, the time for aerodynamic lift to change after an abrupt flow change is not accurately known. It was not known

whether diffraction phase loads were dominant in causing damage to an aircraft in a nuclear encounter. If they dominated over later aerodynamic flow loads, then better resolution of diffraction phase uncertainties would be necessary. If they were not dominant, then present understanding would be adequate. An investigation of the importance of the diffraction phase loads was made by changing the diffraction phase loads in a nuclear gust response program and determining the resulting effects on structural response.

The structural response was calculated for two different aircraft using the VIBRA-4 code with and without the diffraction phase loads. The results show that although the diffraction phase loads are not large enough to cause major structural damage it is important to include them with the gust loads to determine the structural response. For some vehicles at critical locations the peak bending moment calculated by VIBRA-4 with the diffraction phase loads included were two to three times as large as those calculated without them.

## 2.0 COMPARISON OF DIFFRACTION PHASE METHODS

Several methods have been developed and documented to handle loads on air vehicles due to nuclear blast. A few of the methods are described briefly below. Many more methods and/or computer programs exist within the many private companies that are concerned with the effects on air vehicles of nuclear blast.

### 2.1 DNA 2048H-1

A general description of structural analysis for gust response and for diffraction phase response is described in Section III-3.3 of the Handbook for Analysis of Nuclear Weapon Effects on Aircraft (Reference 7). In this reference "overpressure effects" describes the same loading which is called diffraction phase loading in this document.

In general this reference separates the effects of gust response and the effects of the diffraction phase loads. Because of the duration of each type of loading and the structural damage caused by each type of loading, the analyst can consider them separately. For the hand calculations described and the accuracies which these methods yield the above assumption may be a valid assumption.

### 2.2 NOVA-2

The NOVA-2 digital computer program (Reference 4) is an extension of the NOVA program, and is one of the Method 2 calculations described in DNA 2048H-1. The NOVA and NOVA-2 programs are digital programs to calculate the linear or non-linear response of localized aircraft structures to overpressure or diffraction phase loads. For these programs the gust response time is long compared to the structural response of interest and therefore is not included in the program.

### 2.3 VIBRA-4

The VIBRA-4 digital computer program (Reference 1) is one of the Method 1 calculations described in DNA 2048H-1. This program is primarily a gust

response program. However the aerodynamic forces include an abrupt change due to shock arrival and passage over a surface. The rest of the computation time is for gust response. This is the program selected for this study. The VIRRA-4 program used for this study is more fully described in Section 3.0.

#### 2.4 VIBRA-6

The VIBRA-6 digital computer program (Reference 5) is an extension of the VIRRA-4 methodology. VIBRA-6 is a new program which uses doublet lattice aerodynamic theory. The program makes the calculations in the frequency domain and uses a Fourier transform to generate the time histories of the gust response. In Section II-4 of Volume II (Reference 6) of the VIBRA-6 documentation it states that VIRRA-6 currently does not contain the equations to include the effects of the diffraction phase loading. The results shown in Section 4.0 of this study show that the equations in Appendix A of Reference 6 should be added to the VIBRA-6 program.

### 3.0 GUST ANALYSIS METHODOLOGY

The gust environment associated with a nuclear burst is manifested by a sudden change in local density and relative wind velocity as the shock wave sweeps across the aircraft. These density and velocity changes result in two distinct types of loading on the aircraft lifting surfaces and fuselage.

The first is called the diffraction loading and lasts approximately the time required for the shock wave to travel one chord of the aerodynamic surface being considered. During this time, the flow is two-dimensional and the normal force coefficient is given by  $C_n = 4/M$ , where  $M$  is the free stream Mach number based on conditions behind the shock front.

The second part of the loading is obtained by considering the three-dimensional lift buildup due to circulation effects. During rapid loading provided by the material velocity, the lift circulation follows a buildup given by a relationship similar to the Wagner function. This buildup in lift is actually a family of curves depending upon the angle of attack of the local lifting section and the chord. Since the material velocity affects all the aerodynamic surfaces almost simultaneously, analysis of an aircraft in this environment must consider the complete aircraft. Another reason why the analysis must consider the complete craft is that the gust may engulf one part (e.g., right wing tip) and affect the position and orientation of other points (e.g., left wing tip) before the shock arrives at that point. Similarly, loading subsequent to the arrival of the shock wave depends upon the elasticity of the aircraft and interaction of each major component upon the other.

Therefore, to assess the vulnerability of the aircraft in a gust environment, a dynamic model must be developed which is actually a mathematical description representing the elastic and inertia properties of the aircraft once transient aerodynamic loads are applied to the lifting surfaces. In addition, the analysis must be achieved using computerized techniques if timely analyses are to be conducted. The computerized technique used in this analysis is described in Reference 1. The method is given the name VIBRA-4, and although it is described in detail in the cited references, a brief description of the methodology will be given to provide an understanding and evaluation of changes

to the technique which were made during the course of this analysis. The equations of motion are described first, followed by a discussion of the aerodynamic loading methodology and finally, a discussion of failure criterion.

### 3.1 VIBRA-4 EQUATIONS OF MOTION

The equations of motion used in VIBRA-4 are derived from Lagrange's equation, which is given by

$$\frac{d}{dt} \left( \frac{\partial T}{\partial \dot{q}} \right) - \frac{\partial T}{\partial q} + \frac{\partial V}{\partial q} = Q_q \quad (1)$$

where

- T is the kinetic energy of the system
- V is the potential energy of the system
- q is any generalized coordinate of the system
- $Q_q$  is the generalized force associated with the coordinate q

The kinetic energy term will be described first, followed by the potential energy term and the generalized force.

#### 3.1.1 Kinetic Energy

The kinetic energy term in Equation 1 is of the form

$$T = 1/2 \sum_{i=1}^n m_i v_i^2 \quad (2)$$

where

- $m_i$  is the  $i^{\text{th}}$  mass of the system of discrete masses describing the mass distribution of the system
- $v_i$  is the linear velocity of the  $i^{\text{th}}$  mass point of the system
- n is the number of masses describing the complete system
- T is the kinetic energy of the system with respect to a reference point, specifically the center of gravity

In component form, Equation 2 may be written

$$T = 1/2 \sum_{i=1}^n m_i \left[ v_{\bar{x}_i}^2 + v_{\bar{y}_i}^2 + v_{\bar{z}_i}^2 \right] \quad (3)$$

where

$v_{\bar{x}_i}$ ,  $v_{\bar{y}_i}$ , and  $v_{\bar{z}_i}$  represent the components of the velocity of mass at point  $i$  in an earth fixed axis system

Figure 1 gives the relationship between the fixed aircraft axis system (FAAS), the moving aircraft axis system (MAAS) and the earth fixed axis system (EFAS).

Since the velocity terms in Equation 3 are along directions of the FAAS, the velocity must be written in terms of the velocity of the reference point plus the velocity of the  $i^{\text{th}}$  mass point relative to the reference point. These component velocities are given in Equation 4.

$$\begin{aligned} v_{\bar{x}_i} &= \dot{\bar{x}}_0 + \dot{\bar{l}}_{x_i} \\ v_{\bar{y}_i} &= \dot{\bar{y}}_0 + \dot{\bar{l}}_{y_i} \\ v_{\bar{z}_i} &= \dot{\bar{z}}_0 + \dot{\bar{l}}_{z_i} \end{aligned} \quad (4)$$

where

$\dot{\bar{x}}_0$ ,  $\dot{\bar{y}}_0$  and  $\dot{\bar{z}}_0$  are the velocity components of the reference point, center of gravity

$\dot{\bar{l}}_{x_i}$ ,  $\dot{\bar{l}}_{y_i}$  and  $\dot{\bar{l}}_{z_i}$  are the relative velocities of the mass point  $i$  with respect to the reference point

The time derivative of Equation 4 is

$$\begin{aligned} \frac{\partial v_{\bar{x}_i}}{\partial t} &= \ddot{\bar{x}}_0 + \ddot{\bar{l}}_{x_i} \\ \frac{\partial v_{\bar{y}_i}}{\partial t} &= \ddot{\bar{y}}_0 + \ddot{\bar{l}}_{y_i} \\ \frac{\partial v_{\bar{z}_i}}{\partial t} &= \ddot{\bar{z}}_0 + \ddot{\bar{l}}_{z_i} \end{aligned} \quad (5)$$

where

$\ddot{x}_0, \ddot{y}_0$  and  $\ddot{z}_0$  are the components of acceleration of the reference point in the FAAS

$\ddot{\bar{x}}_i, \ddot{\bar{y}}_i$  and  $\ddot{\bar{z}}_i$  are the components of acceleration of mass point  $i$  relative to the reference point in the FAAS

The values of  $\ddot{\bar{x}}_i, \ddot{\bar{y}}_i$  and  $\ddot{\bar{z}}_i$  are obtained in the following manner. The accelerations of mass points will be calculated in the moving aircraft system, therefore, a coordinate transformation from the MAAS system to the FAAS is required. Using the coordinates of the mass point in the FAAS and the MAAS to be  $\bar{x}_i, \bar{y}_i, \bar{z}_i$  and  $x_i, y_i, z_i$ , respectively; and applying an Euler transformation the following is obtained

$$\begin{aligned} \bar{x}_i = & x_i (\cos \bar{\theta} \cos \bar{\psi}) + y_i (\sin \bar{\beta} \sin \bar{\theta} \cos \bar{\psi} + \cos \bar{\beta} \sin \bar{\psi}) \\ & + z_i (-\cos \bar{\beta} \sin \bar{\theta} \cos \bar{\psi} + \sin \bar{\beta} \sin \bar{\psi}) \end{aligned} \quad (6)$$

$$\begin{aligned} \bar{y}_i = & x_i (-\cos \bar{\theta} \sin \bar{\psi}) + y_i (\cos \bar{\beta} \cos \bar{\psi} - \sin \bar{\beta} \sin \bar{\theta} \sin \bar{\psi}) \\ & + z_i (\sin \bar{\beta} \cos \bar{\psi} + \cos \bar{\beta} \sin \bar{\theta} \sin \bar{\psi}) \end{aligned}$$

$$\bar{z}_i = x_i \sin \bar{\theta} - y_i (\sin \bar{\beta} \cos \bar{\theta}) + z_i (\cos \bar{\beta} \cos \bar{\theta})$$

where

$\bar{\theta}, \bar{\beta}, \bar{\psi}$  are the rigid body rotation angles of the reference point in the FAAS.

Equation 6 is then differentiated twice with respect to time to obtain the relationship between the relative accelerations in the FAAS and the MAAS. The next step is to obtain the rotational accelerations in the FAAS in terms of rotations in the MAAS. These relationships become

$$\begin{aligned} \bar{\beta} &= \beta - \psi\theta \\ \bar{\theta} &= \theta + \psi\beta \\ \bar{\psi} &= \psi - \theta\beta \end{aligned} \quad (7)$$

Making these substitutions into the acceleration equations resulting from the differentiation of Equation 6 and letting the FAAS and the MAAS be coincident at any instant of time, a substantial simplification in the equations (i.e., all

cosine terms become 1.0 and all sine terms become 0.0) can be made.

The final equation becomes

(8)

$$\ddot{l}_{x_i} = \ddot{l}_{x_i} + l_{y_i} \ddot{\psi} - l_{z_i} \ddot{\theta} + 2\dot{l}_{y_i} \dot{\psi} - 2\dot{l}_{z_i} \dot{\theta} - l_{x_i} (\dot{\theta}^2 + \dot{\psi}^2) + \dot{\beta} (l_{y_i} \dot{\alpha} + l_{z_i} \dot{\psi})$$

$$\ddot{l}_{y_i} = \ddot{l}_{y_i} - l_{x_i} \ddot{\psi} + l_{z_i} \ddot{\beta} - 2\dot{l}_{x_i} \dot{\psi} + 2\dot{l}_{z_i} \dot{\beta} - l_{y_i} (\dot{\beta}^2 + \dot{\psi}^2) + \dot{\theta} (l_{x_i} \dot{\beta} + l_{z_i} \dot{\psi})$$

$$\ddot{l}_{z_i} = \ddot{l}_{z_i} + l_{x_i} \ddot{\theta} - l_{y_i} \ddot{\beta} + 2\dot{l}_{x_i} \dot{\theta} - 2\dot{l}_{y_i} \dot{\beta} - l_{z_i} (\dot{\beta}^2 + \dot{\theta}^2) + \dot{\psi} (l_{x_i} \dot{\beta} + l_{y_i} \dot{\theta})$$

One final step is taken as part of the normal mode approach. Let the coordinate of a mass point at any instant of time be the original coordinate plus its modal displacement as shown in Equation 9

$$\begin{aligned} l_{x_i} &= l_{x_{i_0}} + \sum_{r=1}^{n_E} \phi_{x_i}(r) q_r \\ l_{y_i} &= l_{y_{i_0}} + \sum_{r=1}^{n_E} \phi_{y_i}(r) q_r \\ l_{z_i} &= l_{z_{i_0}} + \sum_{r=1}^{n_E} \phi_{z_i}(r) q_r \end{aligned} \quad (9)$$

where

$l_{x_{i_0}}, l_{y_{i_0}}, l_{z_{i_0}}$  are the coordinates of mass  $i$  when the aircraft is undeformed

$n_E$  is the number of elastic modes

$q_r$  is the deflection of the  $r^{\text{th}}$  mode

$\phi_{x_i}(r), \phi_{y_i}(r), \phi_{z_i}(r)$  are the modal deflections in the  $r^{\text{th}}$  mode of mass point  $i$

The first and second time derivatives of these coordinates then become

$$\dot{x}_i = \sum_{r=1}^{n_E} \phi_{x_i}(r) \dot{q}_r \quad (10)$$

$$\dot{y}_i = \sum_{r=1}^{n_E} \phi_{y_i}(r) \dot{q}_r$$

$$\dot{z}_i = \sum_{r=1}^{n_E} \phi_{z_i}(r) \dot{q}_r$$

and

$$\ddot{x}_i = \sum_{r=1}^{n_E} \phi_{x_i}(r) \ddot{q}_r$$

$$\ddot{y}_i = \sum_{r=1}^{n_E} \phi_{y_i}(r) \ddot{q}_r \quad (11)$$

$$\ddot{z}_i = \sum_{r=1}^{n_E} \phi_{z_i}(r) \ddot{q}_r$$

A similar procedure is used to relate the rigid body translational accelerations in the FAAS and MAAS. The resulting equations are

$$\begin{aligned} \ddot{\bar{x}}_0 &= \ddot{x}_0 + \dot{\psi} \dot{y}_0 - \dot{\theta} \dot{z}_0 \\ \ddot{\bar{y}}_0 &= \ddot{y}_0 + \dot{\beta} \dot{z}_0 - \dot{\psi} \dot{x}_0 \\ \ddot{\bar{z}}_0 &= \ddot{z}_0 - \dot{\beta} \dot{y}_0 + \dot{\theta} \dot{x}_0 \end{aligned} \quad (12)$$

Equation 12 is found by differentiating the relationship between velocities in the FAAS and the MAAS, which are similar in form to those of Equation 6, and applying the simplification of assuming that the FAAS and MAAS are coincident at any instant of time. One other set of equations is needed to support Equation 12. This is the set of equations relating the rigid body rotational velocities in the fixed and moving systems. These equations become

$$\begin{aligned} \dot{\beta} &= \dot{\bar{\beta}} + \dot{\psi} \sin \bar{\theta} \\ \dot{\theta} &= \dot{\bar{\theta}} \cos \bar{\beta} - \dot{\psi} \cos \bar{\theta} \sin \bar{\beta} \\ \dot{\psi} &= \dot{\bar{\theta}} \sin \bar{\beta} + \dot{\psi} \cos \bar{\theta} \cos \bar{\beta} \end{aligned} \quad (13)$$

### 3.1.2 Potential Energy

The potential energy of the system is composed of the potential energy contributed by the elastic vibratory modes of the structure and that resulting from gravitational forces. The contribution from the elastic vibratory modes of the structure may be written as

$$V_v = 1/2 \sum_r M_r \omega_r^2 q_r^2 \quad (14)$$

where

$M_r$  is the generalized mass associated with the  $r^{\text{th}}$  normal mode of the system

$$M_r = \sum_{i=1}^n m_i \left\{ \left[ \phi_{x_i}^{(r)} \right]^2 + \left[ \phi_{y_i}^{(r)} \right]^2 + \left[ \phi_{z_i}^{(r)} \right]^2 \right\}$$

$\omega_r$  vibrational frequency of the  $r^{\text{th}}$  normal mode

$q_r$  is the  $r^{\text{th}}$  normal coordinate

$r$  represents the  $r^{\text{th}}$  normal mode of the system

Equation 15 gives the contribution from gravitational forces

$$V_g = \sum_i m_i g \left[ (\bar{x}_0 + l_{x_i}) \sin \bar{\theta}_E - (\bar{y}_0 + l_{y_i}) \right. \quad (15)$$

$$\left. \sin \bar{\beta}_E \cos \bar{\psi}_E + (\bar{z}_0 + l_{z_i}) \cos \bar{\beta}_E \cos \bar{\psi}_E \right]$$

where

$\bar{\theta}_E, \bar{\beta}_E, \bar{\psi}_E$  are the Euler angles relating the coincident axes to the Earth Fixed Axis

$m_i$  represents the  $i^{\text{th}}$  mass of the system

The total potential energy then becomes

$$V = V_v + V_g \quad (16)$$

### 3.1.3 Generalized Forces

The generalized force associated with the coordinate  $q$  may be represented by

$$Q_{q_r} = \frac{\partial W}{\partial q_r} \quad (17)$$

where

$W$  represents the virtual work of the system  
 $q_r$  is the  $r^{\text{th}}$  generalized coordinate

The partial derivative of the virtual work is given by

$$\frac{\partial W}{\partial q_r} = F_x \frac{\partial \dot{x}_i}{\partial \dot{q}_r} + F_y \frac{\partial \dot{y}_i}{\partial \dot{q}_r} + F_z \frac{\partial \dot{z}_i}{\partial \dot{q}_r} \quad (18)$$

where

$F_x, F_y, F_z$  are the external forces (aerodynamic, etc.) acting on the system

### 3.1.4 Equation of Motion

Using the components presented in the previous paragraphs and conducting the operations given by Equation 1, the equation of motion used in VIRRA-4 is obtained.

$$\begin{aligned} & \sum_{i=1}^n m_i \left\{ \phi_{x_i}^{(r)} \frac{\partial v_{x_i}}{\partial t} + \phi_{y_i}^{(r)} \frac{\partial v_{y_i}}{\partial t} + \phi_{z_i}^{(r)} \frac{\partial v_{z_i}}{\partial t} \right\} + M_r \omega_r^2 q_r \\ & + \sum_{i=1}^n m_i g \left\{ \phi_{x_i}^{(r)} \sin \theta_e - \phi_{y_i}^{(r)} \sin \beta_E \cos \bar{\theta}_E + \phi_{z_i}^{(r)} \cos \bar{\beta}_E \cos \bar{\theta}_E \right\} \\ & = \sum_{i=1}^n \left\{ F_{x_i} \phi_{x_i}^{(r)} + F_{y_i} \phi_{y_i}^{(r)} + F_{z_i} \phi_{z_i}^{(r)} \right\} \end{aligned} \quad (19)$$

where the components of Equation 19 are previously defined. Equation 19 and its supporting equations may be written as

$$[M_{rs}] (\ddot{q}_s) = (RHS_r) \quad (20)$$

where

$RHS_r$  (righthand side) is a function of velocities and displacements and may be found by the previously defined equation

$\ddot{q}_s$  is the modal acceleration components

$M_{rs}$  is the generalized mass matrix

The solution procedure is accomplished by solving for the acceleration of the generalized coordinates and integrating these components to determine velocities and displacements. The integration is conducted numerically by a fifth-order Adams integration formula.

### 3.2 AERODYNAMIC LOADING

The forces  $F_x$ ,  $F_y$ , and  $F_z$  given in equation 19 are comprised of two distinct sources of aerodynamic loadings. The first is the 1g flight loads which are normally acting on the aircraft and the second is the incremental loading produced by changes in material velocity and density behind the shock wave. The VIBRA-4 program was modified in this area of steady loading. These changes (made by AFWL) will be described below. This version of the VIBRA-4 program was restricted to subsonic aerodynamics only. The previous versions of the program did not consider a variation in the ratio of lift coefficient to angle of attack across the span of components and it assumed that the center of pressure was located at the 50 percent chord for steady loads as well as the unsteady load where 50 percent is appropriate. Modifications were made to set the center of pressure at the 40 percent chord which was a compromise between the 1g flight condition and the unsteady load condition. A subsonic load subroutine (Weissinger method) documented in Reference 9 was added to the VIBRA-4 program to provide the steady airload distribution calculations.

To determine the 1g flight loads, the program adjusts the wing and horizontal stabilizer angle of attack to provide a balanced load condition. During this

iteration period, the structure is allowed to deflect as its modal coefficient allow it. At the end of the steady flight calculation, the forces acting on the aircraft are completely balanced and the loads at each of the desired locations are calculated.

The second component of aerodynamic loading results from the material velocity behind the shock wave. The model for calculating the overpressure and the associated material velocity components for a given yield and range is discussed in detail in Section 2.3. The material velocity time history induces a time-dependent angle of attack which causes time-dependent load to exist in the aircraft structure. The instantaneous angle of attack is calculated by assigning three of the discrete masses, either within or near an aerodynamic strip, to each of the aerodynamic panels so that a plane passed through the masses represents the orientation of a particular strip. The unit normal vector for this plane is then found, and the angle of attack determined by forming the dot product of this vector with the velocity vector of the surface relative to the air. The angle is measured in a plane containing both the velocity and the normal vector. Equation 21 shows this relationship.

$$N \cdot V_A = |N| |V_A| \cos (90^\circ + \alpha) = |N| |V_A| \sin \alpha \quad (21)$$

where

$N$  is the normal vector

$V_A$  is the velocity vector of the aerodynamic strip relative to the air

$\alpha$  is the angle of attack

Once the angle of attack or change in angle of attack ( $\alpha - \alpha_0$ ) is found, the normal force coefficient can then be determined. Subsequently, the lift force is determined from Equation 22.

$$L_A = 1/2 \rho V_A^2 C_N S_A \quad (22)$$

where

$L_A$  is the total lift acting on a lifting segment  
 $\rho$  is the density of the air flowing over the surface  
 $V_A$  is the velocity of the aerodynamic strip relative to air  
 $S_A$  is the area of the particular strip

The components of the normal force are then found by multiplying the total force by the components of the unit normal vector. The components are given by

$$\begin{aligned} F_x &= L_A \frac{N_x}{|N|} \\ F_y &= L_A \frac{N_y}{|N|} \\ F_z &= L_A \frac{N_z}{|N|} \end{aligned} \quad (22)$$

These forces are then distributed among the individual masses and the response loop continues.

The normal force coefficients used are from two sources, depending on whether the trim or steady load calculation is being performed, or the unsteady loading due to gust is being performed. As discussed previously, the steady load calculations are achieved by using the Weissinger method. For the unsteady portion of the loading, experimental normal force coefficient data make up the portion of the time when circulation lift is predominant; i.e., after the aerodynamic panel has been completely engulfed by the shock wave. Another way to indicate this time, and the one used in VIBRA-4, is by using the concept of aerodynamic time  $S = Vt/C$ , where  $V$  is the vector sum of the velocity of the lifting surface and the shock front,  $t$  is time, and  $C$  is the structural chord of the lifting panel. When  $S = 0$ , the shock has just arrived at the lifting surface panel. When  $S = 1$ , the panel has been engulfed by the shock. Figure 2 shows the basic two-dimensional unsteady normal forces coefficient to angle of attack ratio as a function of aerodynamic time. These data were obtained in shock tube experiments.

In reviewing the unsteady aerodynamics of the VIBRA-4 program, it was observed

that each lifting surface and lifting surface panel was given the same normal force coefficient to angle of attack ratio; i.e., the value of  $C_N/\alpha$  was constant across the span and for each surface. To avoid this limitation, results of the airload distribution formed during the steady load calculations were saved and used to scale the data of Figure 2 to be more applicable to the lifting surfaces. The net effect of this scaling process is to reduce the total loading slightly and to redistribute the loading across the surface to better match the actual distribution.

Fuselage aerodynamic loading is obtained in a similar manner except that the force is proportional to a cross-flow drag force given by

$$F_N = 0.35 \frac{\rho}{2} V_{N_F} |V_{N_F}| S \quad (24)$$

where

- $F_N$  is the cross-flow drag force in the direction of  $V_{N_F}$
- $\rho$  is the ambient air density at the fuselage aerodynamic segment
- $S$  is the area of the fuselage aerodynamic segment
- $V_{N_F}$  is the flow velocity relative to the aircraft and normal to the fuselage longitudinal axis

No aerodynamic loading is included for the engine nacelles. Inclusion of nacelle aerodynamics should provide damping to the nacelle motion, but it will also provide some limited nacelle loading. It is unknown just how much effect nacelle aerodynamics would make in the present results. A more in-depth study should look into this particular problem and include a more adequate failure moment calculation using combined loads instead of the single-side load presently used.

### 3.3 GUST ENVIRONMENT

A new AFWL 1 KT nuclear standard (Reference 10) based on data from the AFWL SPUTTER and SAP fluid dynamics programs provides the free air overpressure, material velocity, and overdensity waveforms for the blast mode<sup>1</sup>. This nuclear

standard replaces the modified IBM Problem-M data used in the VIBRA-4 blast model. Figure 4 indicates that for overpressures less than 5 to 10 psi, this standard predicts a range which is appreciably shorter than that obtained using the IBM Problem-M data.

Replacing the free-air Problem-M curve with the AFWL 1 KT sea level standard required a modification to two scaled reflection factor curves given in Section II of Reference 1. These factors describe, as a function of range, the blast characteristics in the regions of regular reflection and Mach reflection. The scaled reflection factor CRFRRR is based on height of burst (HOB) curves and applied to the reflection phase of a near-ground burst. A review of HOB overpressure data indicated that the overpressure along the ground in the region of regular reflection could be reproduced effectively by considering an imaginary nuclear explosion with a specified effective yield at the original burst point. The effective yield can be obtained by modifying the actual yield by a reflection factor. In this manner, a curve of the cube root of this reflection factor for the regular reflection region CRFRRR was determined as a function of the slant range to specific points on the ground. Likewise the scaled reflection factor CPERMR was determined for the region of Mach reflection. These factors are used in the blast model to determine the effective yield required to duplicate the overpressure along the ground in the region of regular and Mach reflection.

#### 3.4 FLIGHT LOAD ALLOWABLES

Vulnerability to gust effects is established by determining the burst time/range at which either a limit flight load (sure-safe) or ultimate allowable flight load (sure-kill) is attained at some location in the aircraft structure. The VIBRA-4 code calculates all forces and moments, but currently provides the capability for monitoring only up and down bending moments on the wing, horizontal stabilizer, and aft fuselage and lateral bending moments on the vertical tail, aft fuselage and nacelles. Component stations having the lowest design margins of safety were selected for each component.

The ultimate allowables were calculated by modifying the ultimate loads by the margin of safety, such that the margin of safety is reduced to zero. The

sure-safe limit allowables in this table are two-thirds of the ultimate allowables.

Mission completion for gust response was considered to be very close to the sure-kill response; i.e., if the load is just slightly less than ultimate the structure will not fracture and the component can still carry loads which will allow mission completion. This result is substantiated by a process called "proof test logic" which effectively guarantees that the structure withstands a particular load.

Changes made to the VIBRA-4 code to more accurately treat combined vertical and lateral fuselage loading are discussed below. The program changes accomplished to calculate internal stresses at wing and fuselage stations were disabled for the current study.

The allowables for wing, horizontal and vertical stabilizers and nacelles are pure bending allowables. Since these components, except for the nacelles, act like a beam, the pure bending allowable is probably adequate.

The fuselage allowable, however, is based on a side-bending moment, an up-bending moment and a down-bending moment. The original VIBRA-4 methodology used a combined loading scheme which allowed the combined loading to follow the boundary  $B_1$  in Figure 3. This allowed both the ultimate up or down load to exist with the ultimate side loading. For pure up or down bending or side bending, the result is correct, but for combined loading an elliptical boundary given by  $B_2$  in Figure 3 is the correct solution. Combined loading is shown for example by  $P_1$  which is not acceptable, whereas,  $P_2$  shows an example of a correct result. The ellipse determined from a combination of pure side bending or vertical bending conditions is seen to provide an accurate representation of the family of straight line segments. The equations used in the program for the bending moment ratio  $M/M_{ult}$  are given by

$$R = \sqrt{\left(\frac{M_z}{B_u}\right)^2 + \left(\frac{M_x}{B_s}\right)^2} \quad (25)$$

where

$B_u$  is the allowable up-bending moment  
 $B_s$  is the allowable side-bending moment  
 $M_z$  is the calculated up-bending moment  
 $M_x$  is the calculated side-bending moment  
 $R$  is the ratio of calculated moment to ultimate moment

This equation is valid for up-bending only. If the bending moment is down, the correct equation is

$$R = \sqrt{\left(\frac{M_z}{B_d}\right)^2 + \left(\frac{M_x}{B_s}\right)^2} \quad (26)$$

where

$B_d$  is the allowable down-bending moment

A similar technique should be used for the engine nacelles, but time did not permit working out the proper relationships. Since the nacelles are not generally limiting components, a side bending allowable is considered reasonable.

#### 4.0 DIFFRACTION PHASE LOADS

The question investigated by this study is "What is the importance of including the diffraction phase loads in calculations of structural response to a nuclear gust?" The VIBRA-4 program was chosen for the comparison work. It was the only program investigated which met the needs of the study. The NOVA-II program includes the diffraction phase loads but not the "long" time response of major structural components. The VIBRA-6 program currently does not have the diffraction phase loads incorporated although the equations for them are included in Appendix A of Reference 5.

The VIBRA-4 program was easily changed to bypass the diffraction phase loads. The aerodynamic loads described in Section 3.3 were modified in the following way. The part of the program that tests for the non-dimensional time  $S$ -immersion and calculates the diffractive phase loads was bypassed and the resulting normal force coefficient then used is as shown in Figure 5. This can be compared to Figure 2 which shows the normal force coefficient used with the diffraction phase loading included.

Two different airplanes were analyzed using the version of VIBRA-4 described in Section 3.0. The mathematical model of the KC-135 used for the study is described in Section 4.1. The mathematical model of the 747-200 used as the other aircraft in the study is described in Section 4.2.

Three blast orientations were used for the study; vertical-beneath, vertical-overhead, and lateral-from the right side of the vehicle. The same input data decks were used for the analysis without the diffraction phase loads as described above.

The comparisons between the VIBRA-4 results with diffraction phase loads and the VIBRA-4 results without diffraction phase loads are shown in section 4.4.

##### 4.1 Dynamic Model - KC-135

The mathematical model for the KC-135 used to conduct the present analysis was previously developed and documented in Reference 2. The model consists of a

discrete mass representation of the aircraft inertia properties by 17 total masses; 28 masses on each wing, 8 of which represent the two engines, 20 fuselage masses, 14 masses on each horizontal stabilizer and 18 masses on the vertical stabilizer. The total gross weight represented by these masses is 292,000 lbs. The distribution of masses was selected to represent each elastic axis panel weight, center of gravity and torsional inertia about the elastic axis. The only exceptions were the engine nacelles for which both pitch and roll inertia were matched. The wing masses were initially in the wing chord plane since the VIBRA-4 program requires mass points associated with the aerodynamic panels to be at the same z coordinate. This simplification reduces the model complexity without significantly affecting the vibration characteristics. In addition, the model consists of 15 symmetric and 15 antisymmetric free aircraft coupled modes of vibration. The coefficients of these modes are used in Equation 19 to determine the response of the structure. These modes were derived from vibrational analysis based upon properties formed from the discrete mass representation and the stiffness properties of the structure.

In addition to the inertia and modal data, the mathematical model includes aerodynamic data. In these data, the lifting surfaces and the fuselage are divided into aerodynamic strips or panels. There is a total of 45 aerodynamic panels on the complete aircraft with 11 on each wing, 4 on the fuselage, 6 on each horizontal stabilizer and 7 on the vertical stabilizer. An area and its centroidal coordinates are associated with each panel.

Additional components of the mathematical model include bending moment data for each component, and engine thrust data. The bending moment data consists of the coordinates of the point on the elastic axis of the component where bending calculations are required, and the limiting bending moment at that station. This limiting bending moment can either be the ultimate or catastrophic damage load or it can be the safe, or no damage load. In this way, the response for any desired loading allowable can be obtained. To assist in locating stations on each component, Table 1 provides a cross reference between buttock line, station and percent semispan for each of the bending moment stations. The actual loads used as allowables are shown in Table 2.

TABLE 1  
 KC-135 COMPONENT BENDING MOMENT LOCATIONS FOR GUST ANALYSIS

COMPONENT	STA. NO.	STATION	$\eta$
Wing	1	WBL 157.3	.20
	2	WBL 259.6	.33
	3	WBL 322.5	.409
	4	WBL 503.5	.64
	5	WBL 550.7	.701
Stabilizer	1	SBL 41.2	.172
	2	SBL 80.0	.333
	3	SBL 119.0	.496
Fin	1	BWL 353.3	.204
	2	RWL 402.5	.348
Body	1	BS 1080	
	2	BS 1200	
	3	BS 1360	
Nacelles	1	BWL 174.714	

WBL - Wing Buttock Line

BS - Body Station

SBL - Stabilizer Buttock Line

RWL - Body Waterline

$\eta$  - Percent Semispan

TABLE 2  
KC-135A ALLOWABLE LOADS FOR MAJOR COMPONENTS

COMPONENT	STA. NO.	STATION	ULTIMATE LOAD		100% LIMIT
			$10^6$ in-lb		LOAD $10^6$ in-lb
Wing	1	WBL 157.3	82.7	Up	51.13
			53.6	Dn	35.73
	2	WBL 259.6	51.4	Up	34.27
			34.5	Dn	23.00
	3	WBL 503.5	15.8	Up	26.60
27.3			Dn	18.20	
4	WBL 503.5	15.8	Up	10.53	
		10.3	Dn	6.87	
5	WBL 550.7	12.0	Up	8.0	
		7.8	Dn	5.20	
Fuselage	1	BS 1080	43.3	Up	28.87
			74.6	Dn	49.73
			52.6	Side	35.07
	2	BS 1200	32.1	Up	21.4
			47.3	Dn	31.53
			44.7	Side	29.8
	3	BS 1360	19.8	Up	13.2
			27.4	Dn	18.27
			29.1	Side	19.4
Horizontal Stabilizer	1	SBL 41.23	3.47	Up	2.31
			3.864	Dn	2.576
	2	SBL 80.0	1.875	Up	1.25
			2.333	Dn	1.555
	3	SBL 119.0	1.12	Up	0.747
			1.414	Dn	0.943
Vertical Stabilizer	1	BWL 353.3	4.11	Side	2.74
	2	BWL 402.5	2.34	Side	1.56
Engine Nacelle	Inbd.	BWL 174.7	0.73	Side	0.487
	Outbd.	BWL 174.7	0.666	Side	0.444

WBL - Wing Buttock Line  
BS - Body Station

SBL - Stabilizer Buttock Line  
WL - Water Line

#### 4.2 DYNAMIC MODEL - 747-200

The mathematical model for the 747-200 used to conduct the present analysis was previously developed and documented in Reference 3. The model consists of a discrete mass representation of the aircraft inertia properties by 177 total masses; 49 masses on each wing, 8 of which represent the two engines, 34 fuselage masses, 15 masses on each horizontal stabilizer and 15 masses on the vertical stabilizer. The total gross weight represented by these masses is 795,000 lbs. The distribution of masses was selected to represent each elastic axis panel weight, center of gravity and torsional inertia about the elastic axis. The only exceptions were the engine nacelles for which both pitch and roll inertia were matched. The wing masses were initially in the wing chord plane since the VIBRA-4 program requires mass points associated with the aerodynamic panels to be at the same z coordinate. This simplification reduces the model complexity without significantly affecting the vibration characteristics. In addition, the model consists of 12 symmetric and 12 antisymmetric free aircraft coupled modes of vibration. The coefficients of these modes are used in Equation 19 to determine the response of the structure. These modes were derived from vibrational analysis based upon properties formed from the discrete mass representation and the stiffness properties of the structure.

In addition to the inertia and modal data, the mathematical model includes aerodynamic data. In these data, the lifting surfaces and the fuselage are divided into aerodynamic strips or panels. There is a total of 45 aerodynamic panels on the complete aircraft with 13 on each wing, 4 on the fuselage, 5 on each horizontal stabilizer and 5 on the vertical stabilizer. An area and its centroidal coordinates are associated with each panel.

Additional components of the mathematical model include bending moment data for each component, and engine thrust data. The bending moment data consists of the coordinates of the point on the elastic axis of the component where bending calculations are required, and the limiting bending moment at that station. This limiting bending moment can either be the ultimate (or catastrophic) damage load or it can be the safe, or no damage load. In this way, the response for

TABLE 3

## 747-200 COMPONENT BENDING MOMENT LOCATIONS FOR GUST ANALYSIS

COMPONENT	STA. NO.	STATION	$\eta$
Wing	1	WBL 176.1	.150
	2	WBL 419.1	.357
	3	WBL 584.7	.498
	4	WBL 743.1	.633
	5	WBL 880.5	.750
Stabilizer	1	SBL 100.0	.229
	2	SBL 231.8	.530
Fin	1	BWL 385.15	.052
	2	BWL 537.05	.443
Body	1	BS 1640.	
	2	BS 2180.	
Nacelles	1	BWL 199.9	

WBL - Wing Buttock Line  
 BS - Body Station  
 $\eta$  - Percent Semispan

SBL - Stabilizer Buttock Line  
 BWL - Body Water Line

TABLE 4

## 747-200 ALLOWABLE LOADS FOR MAJOR COMPONENTS

COMPONENT	STA. NO.	STATION	ULTIMATE LOAD		100% LIMIT LOAD	
			10 <sup>6</sup> in-lb		10 <sup>6</sup> in-lb	
Wing	1	WBL 176.1	309.5	Up	206.33	
			283.86	Dn	189.24	
	2	WBL 410.1	179.15	Up	119.43	
			141.56	Dn	94.27	
	3	WBL 584.7	108.39	Up	72.26	
77.26			Dn	49.17		
4	WBL 743.1	56.84	Up	37.29		
		36.14	Dn	24.09		
5	WBL 880.5	24.19	Up	16.13		
		15.35	Dn	10.22		
Fuselage	1	BS 1640.	135.0	Up	80.30	
			320.0	Dn	212.33	
			49.0	Side	32.67	
Horizontal Stabilizer	1	SBL 100.0	14.9	Up	9.93	
			19.1	Dn	12.72	
	2	SBL 231.8	4.6	Up	3.07	
			6.0	Dn	4.00	
Vertical Stabilizer	1	WL 385.15	31.6	Side	1.07	
	2	WL 537.05	7.42	Side	4.95	
Engine Nacelle	Inbd.	WL 199.9	90.3	Side	60.2	
	Outbd.	WL 199.7	72.5	Side	48.33	

WBL - Wing Buttock Line  
BS - Body Station

SBL - Stabilizer Buttock Line  
WL - Water Line

any desired loading allowable can be obtained. To assist in locating stations on each component, Table 3 provides a cross reference between buttock line, station and percent semispan for each of the bending moment stations. The actual loads used as allowables are shown in Table 4.

#### 4.3 COMPARISON OF VIBRA-4 RESULTS

The VIBRA-4 output for each run included the bending moment at several stations for each time increment. At the end of each time history the ratio of the peak load to the allowable load at each station is also printed out.

Table 5 shows the flight condition used for the KC-135 analysis. The time histories are shown in Figures 6 through 19. Most of these show small differences between the VIBRA-4 results and the VIBRA-4 without diffraction phase loads. Table 6 is a summary of the peak bending moment ratios calculated for the KC-135. The summary shows the VIBRA-4 ratios, without diffraction phase loads ratios, and the percent increase in the ratio by including the diffraction phase loading.

TABLE 5  
KC-135 FLIGHT CONDITION

Velocity	729 fps-true
Altitude	20,000 feet
Overpressure	1.07 psi
Yield	1.0 MT
Material Velocity	110.06 fps
Range	25,000 feet

The 747-200 flight condition analyzed is shown in Table 7. The time histories from this analysis are shown in Figures 20 through 38. Like the KC-135 analysis some show only small differences between the VIBRA-4 results and the VIBRA-4 without diffraction phase loads. However the time histories for other stations show vast differences in peak loads between the two sets of results. The summary of peak bending moment ratios in Table 8 show that increases in peak loads of 300 percent were calculated as a result of including the diffraction phase loads.

TABLE 6

## KC-135 PEAK BENDING MOMENT RATIO SUMMARY

	STA. η	BLAST FROM BELOW			BLAST FROM ABOVE			BLAST FROM RIGHT		
		1	2	3	1	2	3	1	2	3
Right Wing	.20	.539	.520	+3.6	.201	.261	+3.8	.276	.269	+2.6
	.33	.616	.598	+3.0	.302	.298	1.3	.323	.307	8.5
	.409	.585	.578	+1.2	.291	.289	0.7	.323	.302	6.9
	.64	.627	.582	+7.7	.280	.253	10.7	.302	.279	8.2
	.701	.563	.509	+10.6	.243	.226	7.5	.276	.256	7.8
Left Wing	.20							.293	.287	2.1
	.33							.349	.325	7.4
	.409							.336	.313	7.3
	.64							.282	.262	7.6
	.701							.266	.238	11.8
Fuselage Station	1080	.494	.358	+38.0	.813	.645	26.0	.352	.259	35.9
	1200	.627	.450	+39.3	.886	.687	28.9	.367	.275	33.5
	1360	.630	.448	+40.6	.841	.636	32.2	.335	.254	31.9
Right Horizontal Stabilizer	.17	.360	.311	+15.7	.378	.398	-5.0	.340	.271	25.5
	.33	.435	.372	+16.9	.574	.516	+11.2	.348	.296	17.6
	.50	.473	.376	+25.8	.733	.565	+29.7	.335	.281	19.2
Left Horizontal Stabilizer	.17							.297	.271	9.6
	.33							.327	.286	14.3
	.50							.315	.265	18.9
Fin	.204							.738	.573	28.8
	.348							.922	.699	31.9

COLUMN 1      VIBRA-4

COLUMN 2      WITHOUT DIFFRACTION PHASE LOADS

COLUMN 3      [COLUMN 1/COLUMN 2 - 1.0] X 100%

Because the user cannot know in advance the effect the diffraction phase loads will have on the total structural response of his system or on the magnitude of change in peak load at any one station, the diffraction phase loads should be included in the structural response calculations for the system.

TABLE 7  
747-200 FLIGHT CONDITION

Velocity	674 fps-true
Altitude	25000 feet
Overpressure	1.67 psi
Yield	5.0 MT
Material Velocity	197.9 fps
Range	30000 feet

TABLE 8

## 747-200 PEAK BENDING MOMENT RATIO SUMMARY

	STA. η	BLAST FROM BELOW			BLAST FROM ABOVE			BLAST FROM RIGHT		
		1	2	3	1	2	3	1	2	3
Right Wing	.150	.482	.417	15.2	.303	.573	-47.1	.342	.328	4.3
	.357	.456	.408	11.9	.317	.560	-43.4	.343	.327	4.7
	.632	.477	.443	7.7	.260	.469	-44.4	.382	.335	13.8
	.750	.625	.460	38.1	.289	.397	-27.3	.409	.343	19.2
Left Wing	.150							.421	.405	4.0
	.262							.428	.397	7.8
	.494							.345	.334	3.2
	.750							.325	.227	14.4
Fuselage Station	1640	.287	.261	-20.5	.572	.450	+27.1	1.783	1.073	66.2
	2180	1.012	.452	+124.0	1.187	.775	+57.1	1.847	.999	84.7
Right Horizontal Stabilizer	.229	.997	.651	53.1	1.200	.774	54.9	.616	.244	152.1
	.530	1.204	.790	52.3	1.368	.853	60.2	.679	.242	180.1
Left Horizontal Stabilizer	.229							.804	.223	259.1
	.530							.834	.219	290.2
Fin	.052							1.842	.442	336.1
	.443							2.598	.641	304.8

COLUMN 1 VIBRA-4

COLUMN 2 WITHOUT DIFFRACTION PHASE LOADS

COLUMN 3 [COLUMN 1/COLUMN 2 - 1.0] x 100%

## 5.0 CONCLUSIONS

The results in Section 4.0 show that the diffraction phase loads should be included in the structural response calculations. The magnitude of the diffraction phase loads was not large enough to change the peak loads alone, but the diffraction phase loads added to the gust loads can have a significant effect on the peak loads calculated. This effect varies from station to station and from one aircraft to another. There is no known rule of thumb or equations that would help the user determine the magnitude of the effect of including diffraction phase loads in the nuclear gust response calculations. Therefore structural response codes such as VIBRA-4 and VIBRA-6 should include the diffraction phase loading with the gust response loading.

## 6.0 RECOMMENDATIONS

1. VIBRA-4 should not be modified to remove the diffraction phase loads.
2. VIBRA-6 should have the diffraction phase loads added.
3. Further studies should be made to determine the effect the diffraction phase loads have on the peak loads with variations in altitude for a given aircraft at various speeds and vice versa.
4. Additional studies should be made to determine the effect the diffraction phase loads have on the peak loads with size of the vehicle. Small air vehicles such as a swept wing fighter and a winged missile such as the Air Launched Cruise Missile (ALCM) could be used for the input models.

## 7.0 REFERENCES

1. AFWL-TR-70-140, Hobbs, N.P., Zartarian, G., Walsh, J.P., A Digital Computer Program for Calculating the Blast Response of Aircraft to Nuclear Explosions, Volume 1, Program Description, April 1971, Air Force Special Weapons Laboratory, Kirtland AFB, NM, 87117.
2. AFWL-TR-72-197, Vol. II, Analytical Models for the B-52H, EC-135A, and 747-200 Aircraft, Shoup, G.S., September 1973 Air Force Weapons Laboratory, Kirtland AFB, NM 87117.
3. AFWL-TR-72-197, Vol. III, Analytical Models for the B-52H, EC-135A, and 747-200 Aircraft, Miller, R.D., September 1973, Air Force Weapons Laboratory, Kirtland AFB, N.M., 87117.
4. AFWL-TR-75-262, Pt. 1, NOVA-2 - A Digital Computer Program for Analyzing Nuclear Overpressure Effects on Aircraft, Part 1, Theory, Lee, W.N., Mente, L.J., August 1976, Air Force Weapons Laboratory, Kirtland AFB, NM, 87117.
5. AFWL-TR-76-210, Vol. 1, Nuclear Blast Response Computer Program, Volume I, Program Description, McGrew, J.A., Giesing, J.P., Kalman, T.P., Croxen, H.H., Rodden, W.P., September 1977, Air Force Weapons Laboratory, Kirtland AFB, N.M. 87117.
6. AFWL-TR-76-210, Vol. II, Nuclear Blast Response Computer Program, Vol. II, Doublet-Lattice and Piston Theory Aerodynamics, Giesing, J.P., Kalman, T.P., Rodden, W.P., Croxen, H.H., McGrew, J.A., September 1977, Air Force Weapons Laboratory, Kirtland AFB, N.M. 87117.
7. DNA 2048H-1 Handbook for Analysis of Nuclear Weapon Effects on Aircraft, Volume I, Staff of Kaman Avidyne, March 1976, Defense Nuclear Agency, Washington, D.C. 20305
8. The Effects of Nuclear Weapons, Glasstone, S., Dolan, P.J., Third Edition 1977, United States Department of Defense and the United States Department of Energy.

9. AFFDL-TR-65-78, Evaluation of Procedures for Calculating Aerodynamic Loads, Schmidel, L.H., May 1965, Air Force Flight Dynamic Laboratory, Wright-Patterson AFB, OH.
10. AFWL-TR-73-55, Nuclear Blast Standard (1 KT), Needham, C.E., et. al., April 1973, Air Force Weapons Laboratory, Kirtland AFB, NM, 87117.

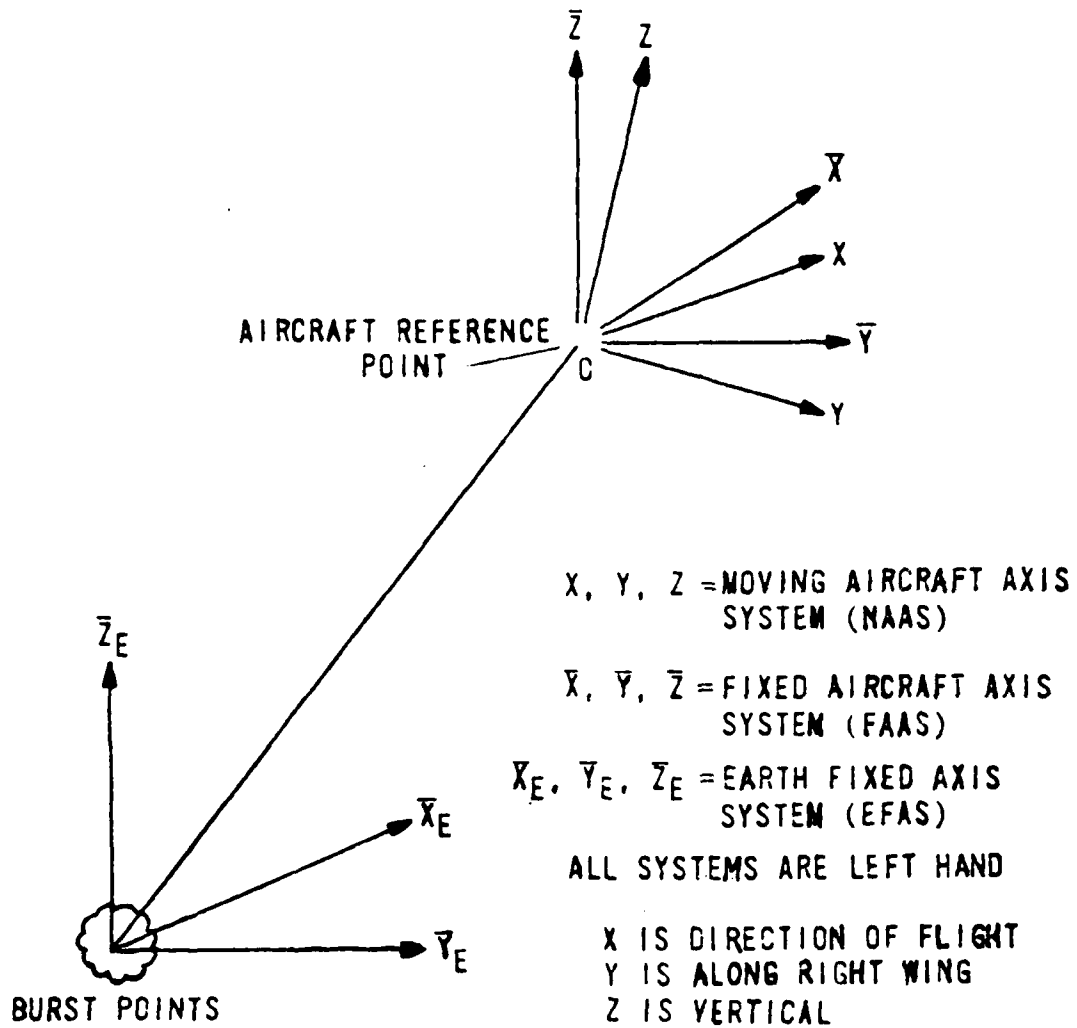


Figure 1 Gust analysis coordinate system.

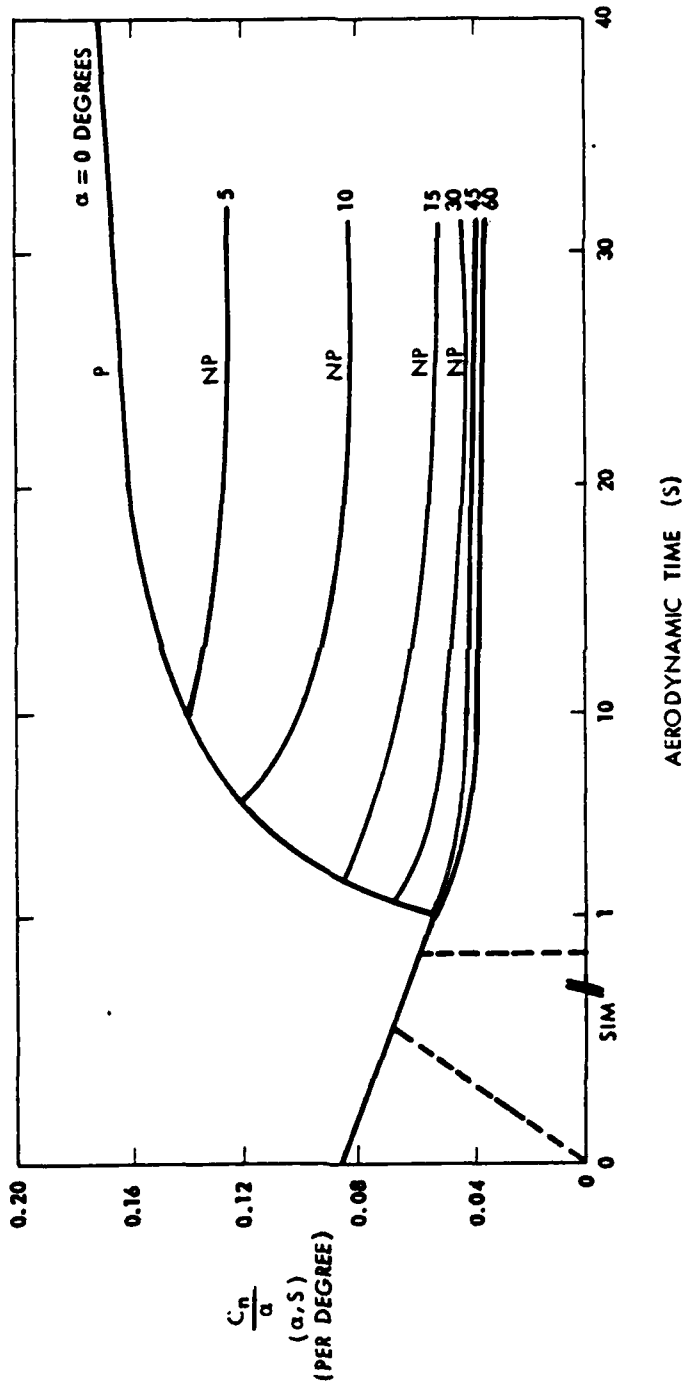
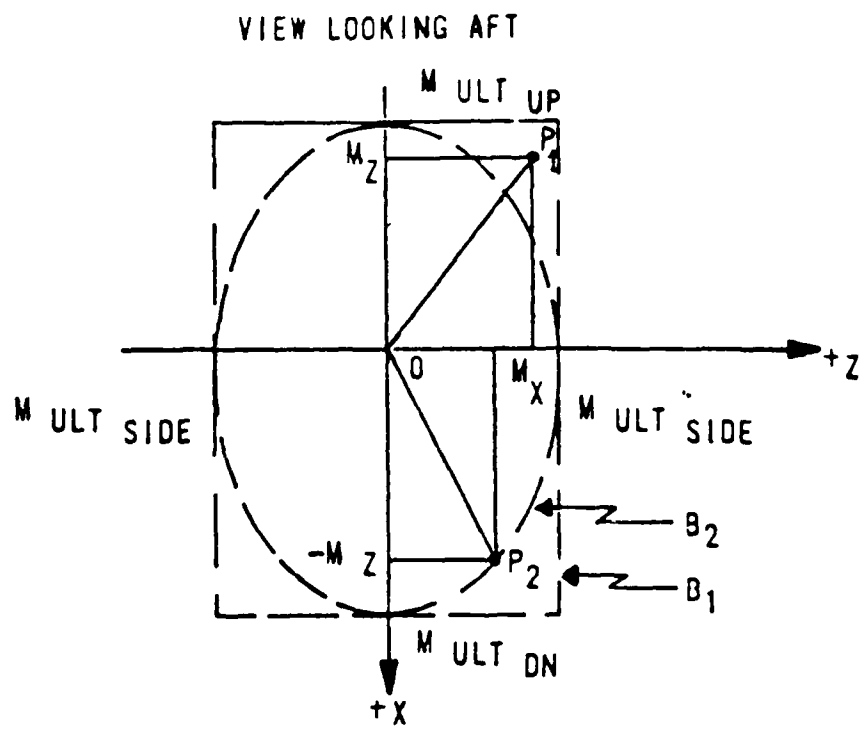


Figure 2 Ratio of two-dimensional normal force coefficient to angle of attack as a function of aerodynamic time



NOTE - AXIS SYSTEM IS VIBRA-4 LOCAL AXIS SYSTEM

Figure 3 Fuselage allowable moment boundary.

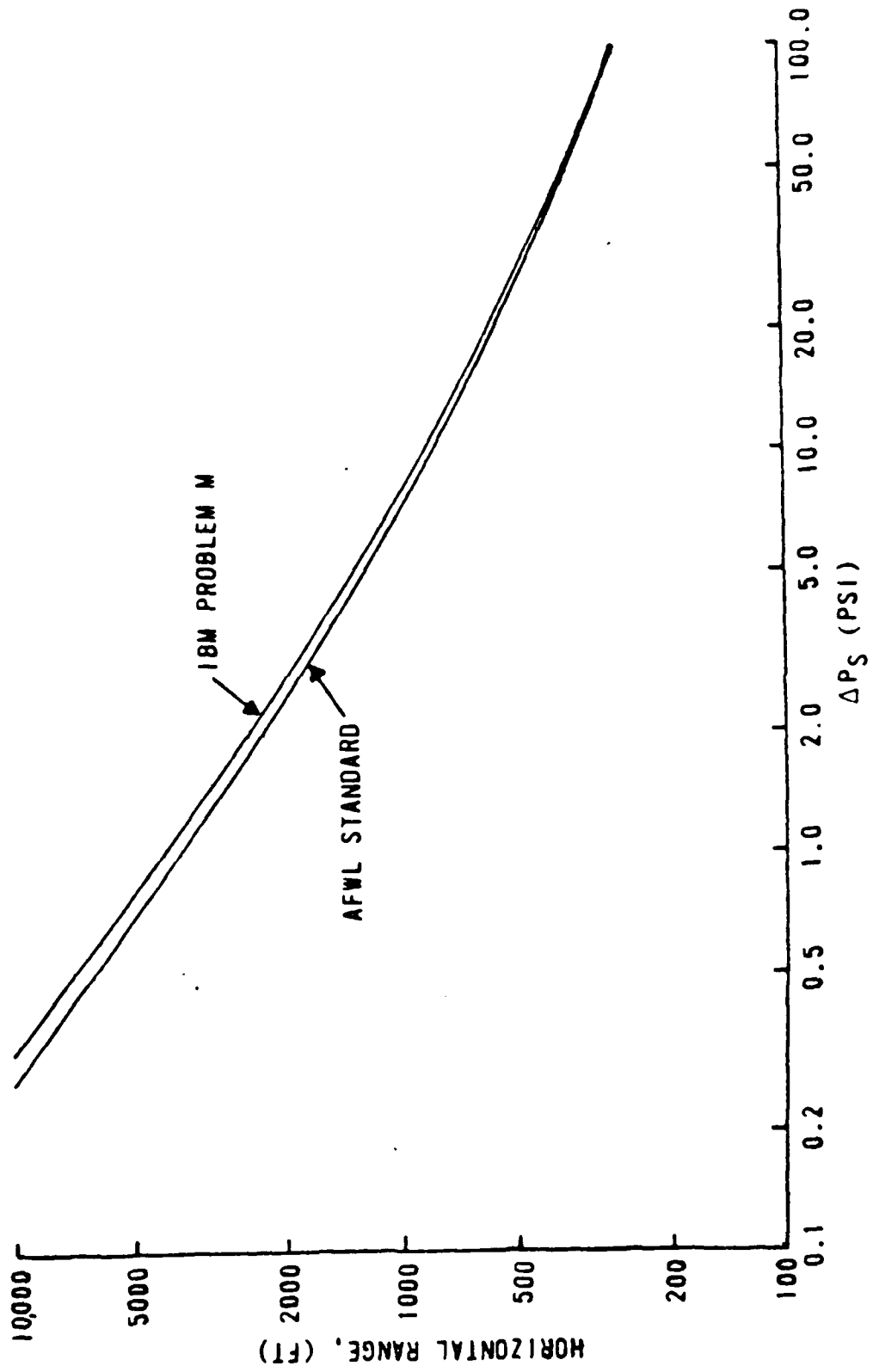


Figure 4 Overpressure as a function of range for a 1-KT explosion at sea level.

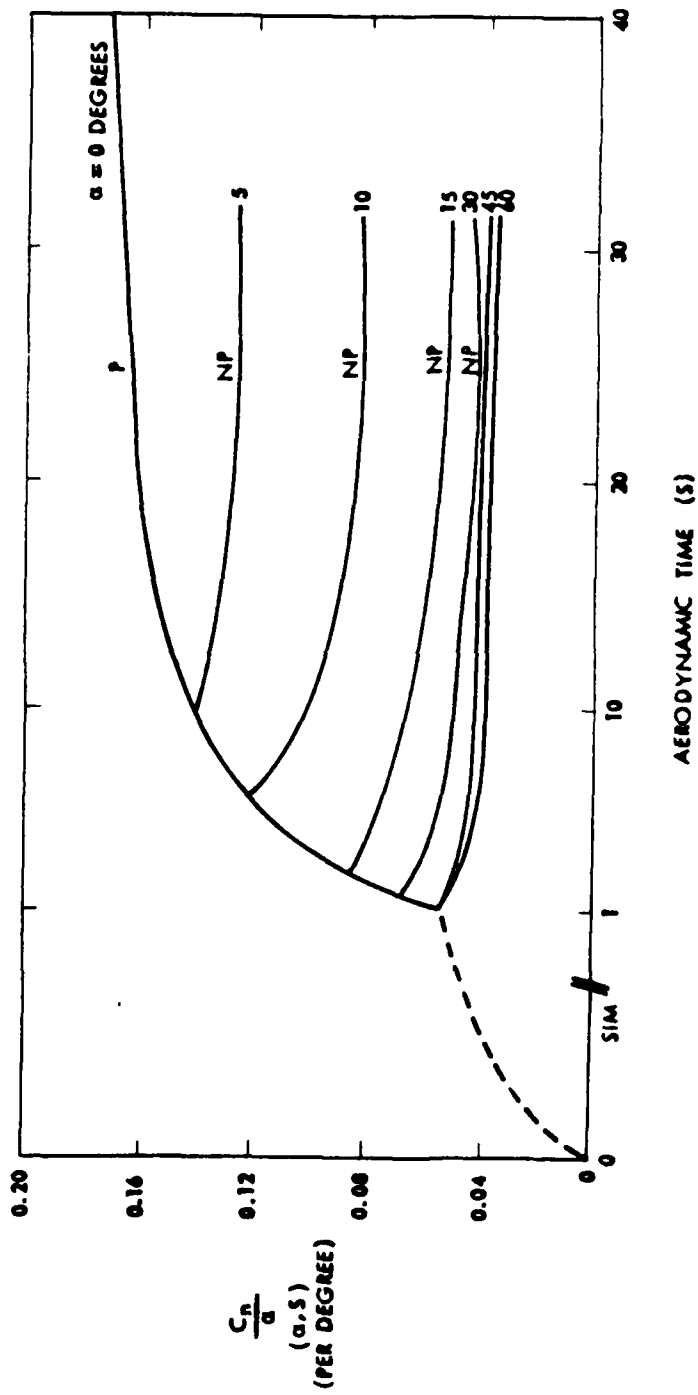


Figure 5 Ratio of two-dimensional normal force coefficient without diffraction phase, to angle of attack as a function of aerodynamic time

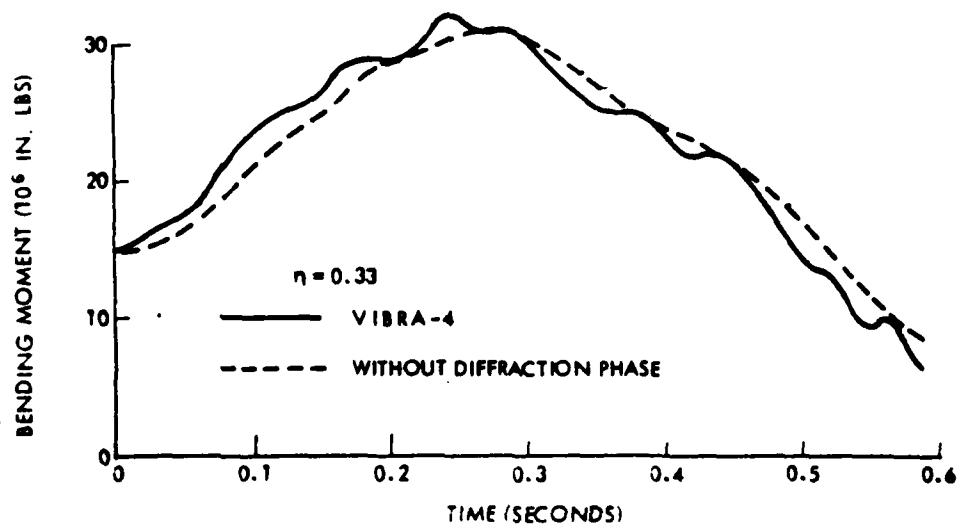
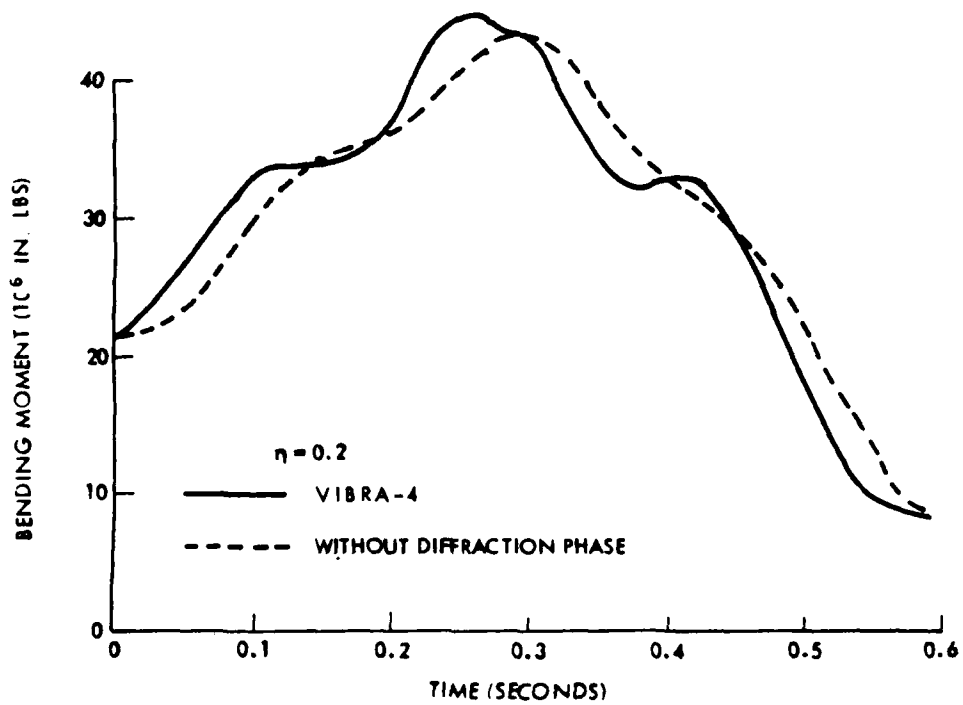


Figure 6 KC-135 right hand wing - blast from below

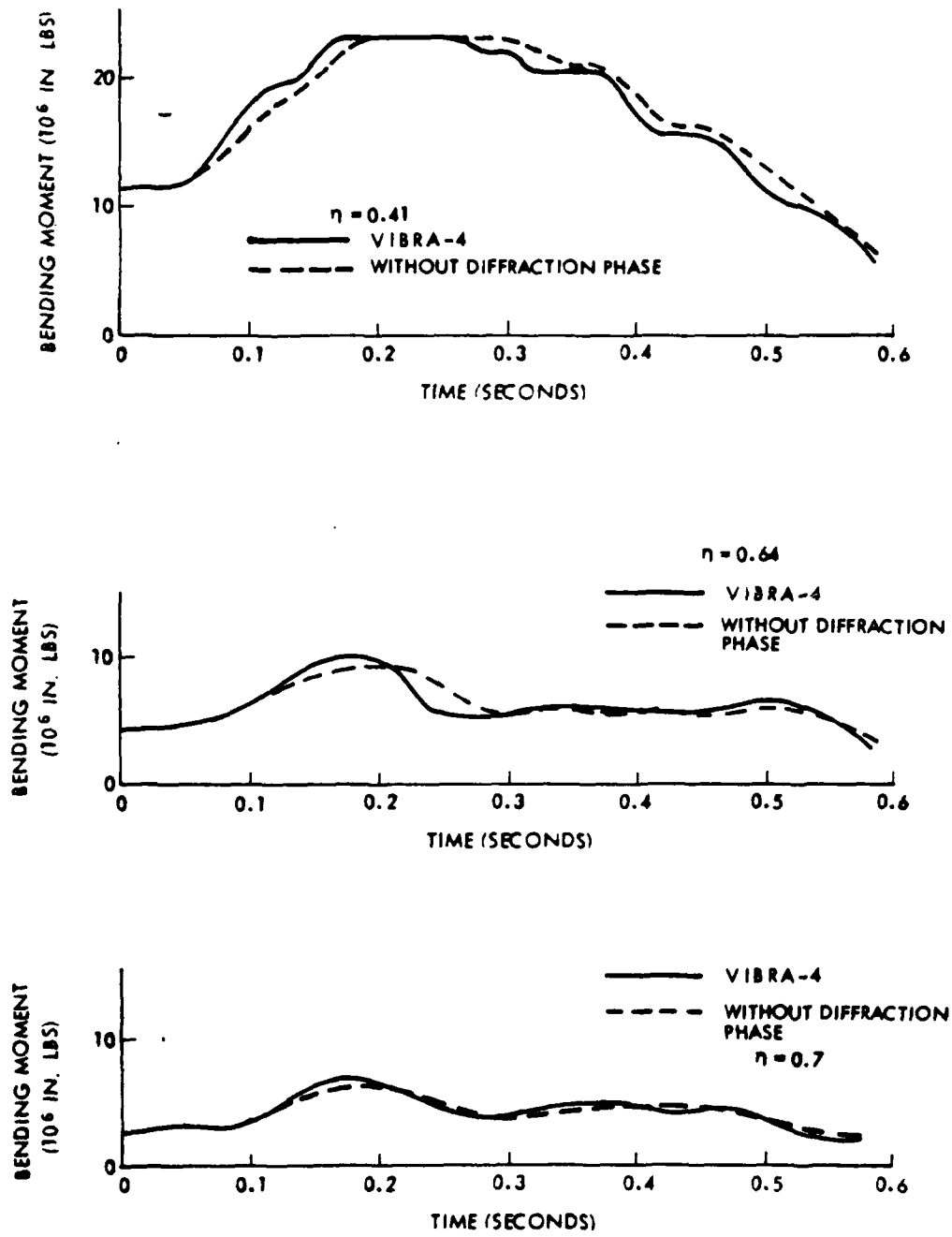


Figure 7 KC-135 right hand wing - blast from below

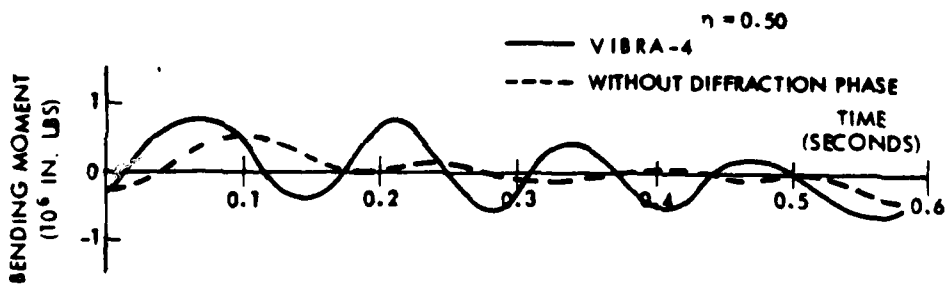
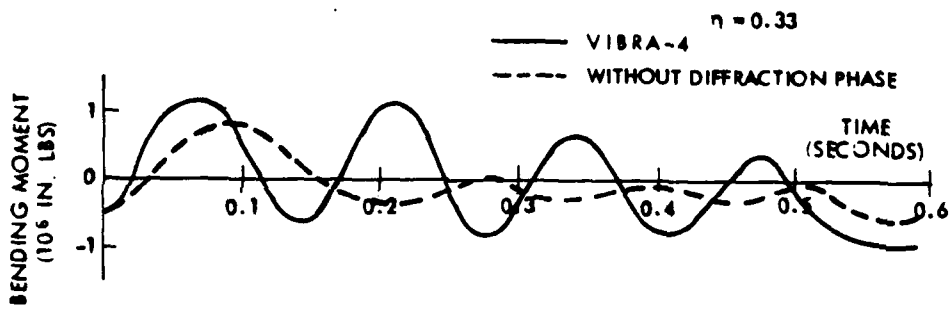
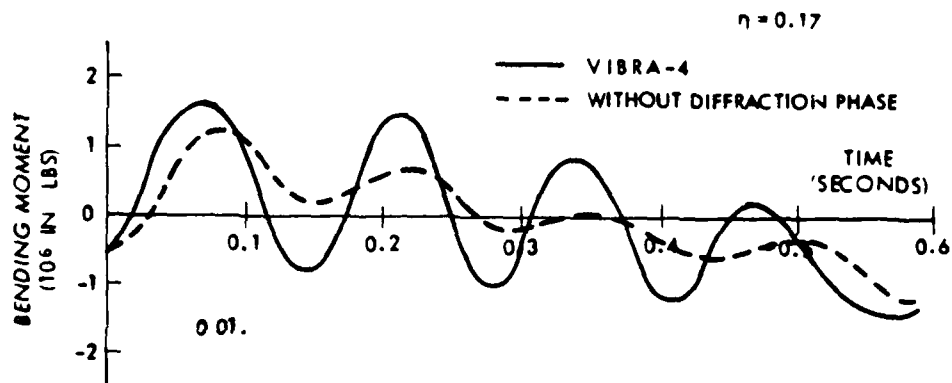


Figure 8 KC-135 right hand horizontal stabilizer - blast from below

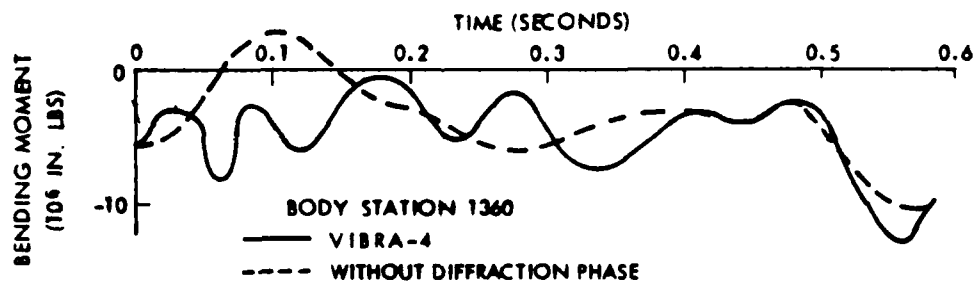
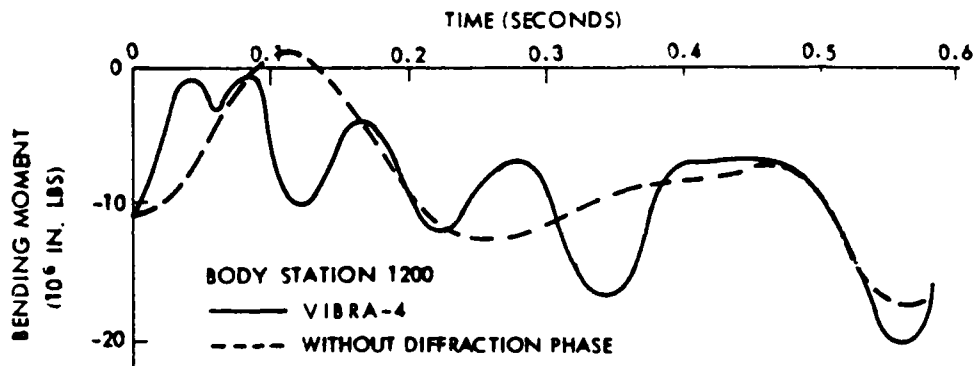
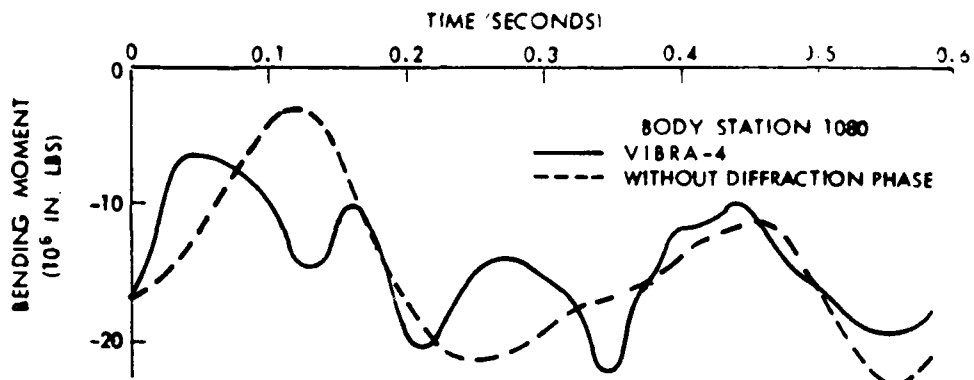


Figure 9 KC-135 body vertical bending - blast from below

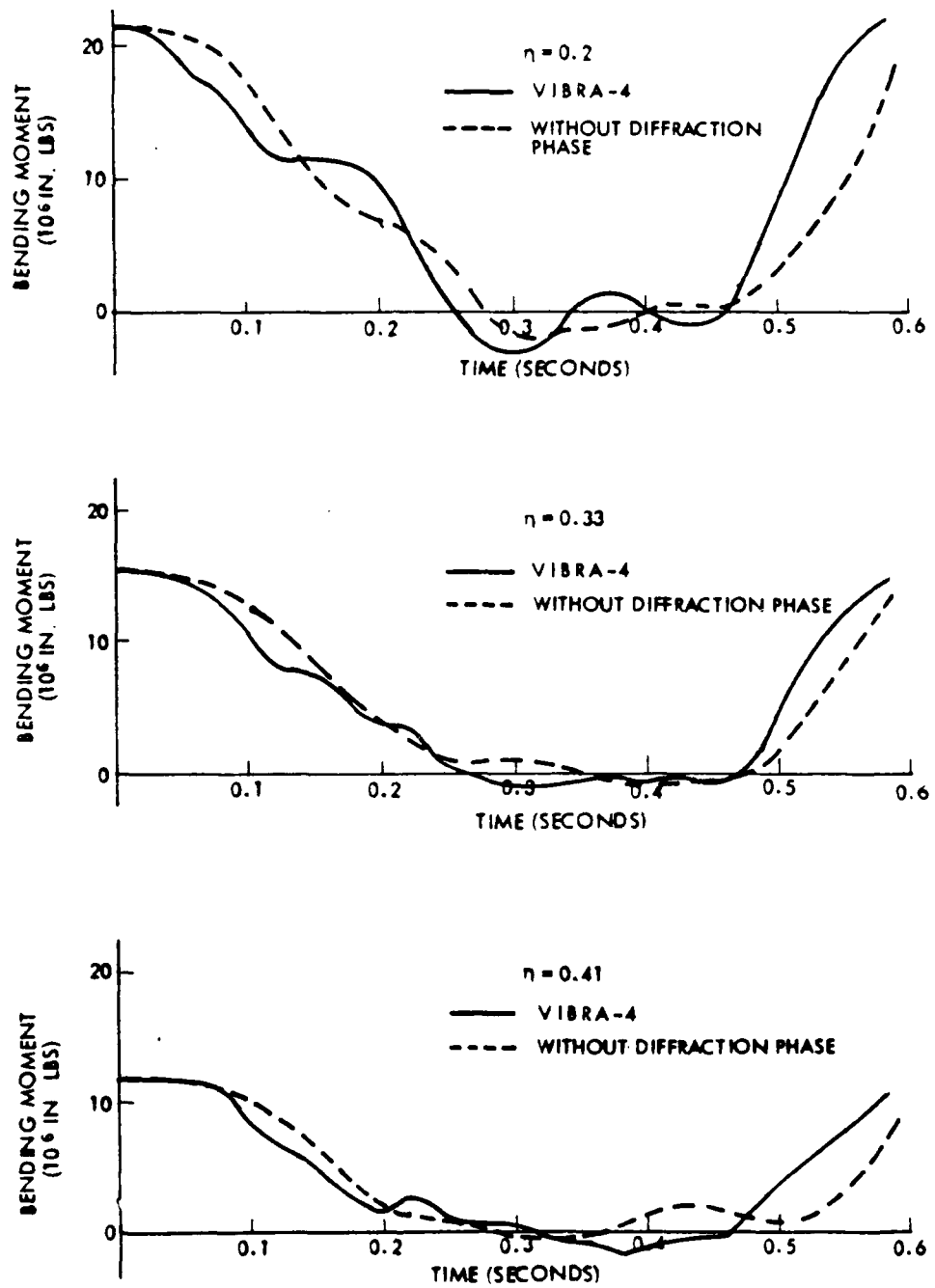


Figure 10 KC-135 right hand wing - blast from above

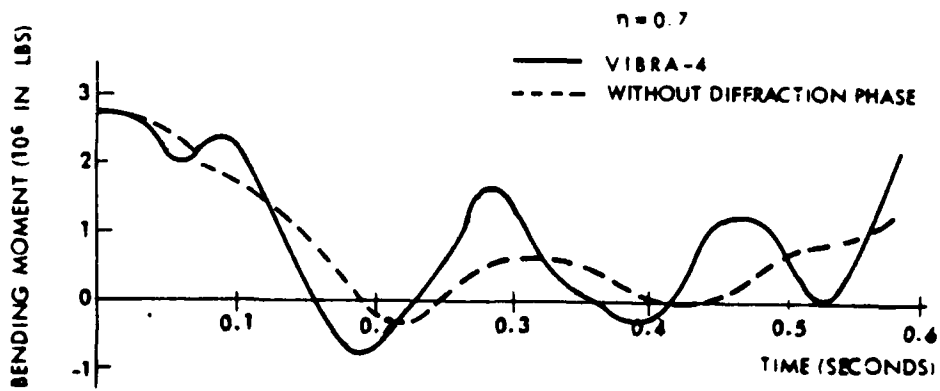
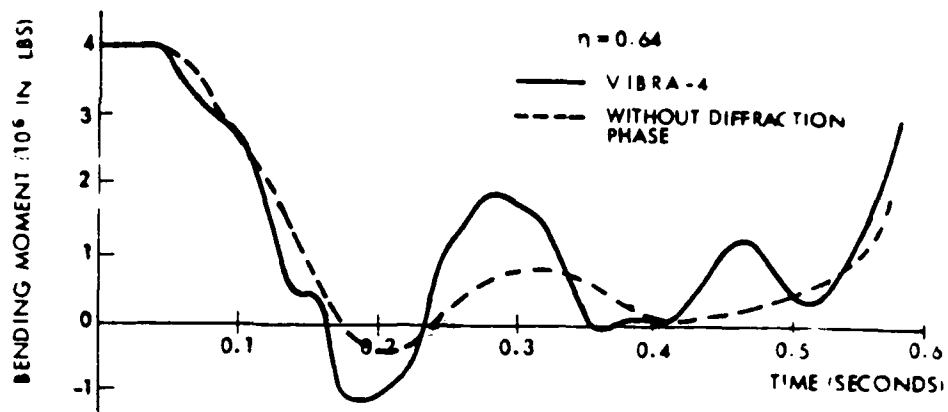


Figure 11 KC-135 right hand wing - blast from above

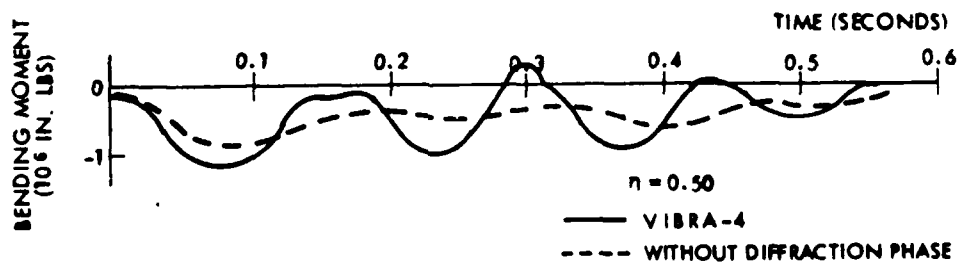
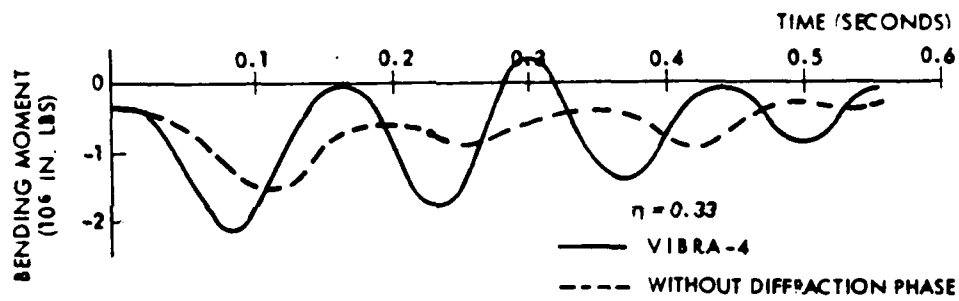
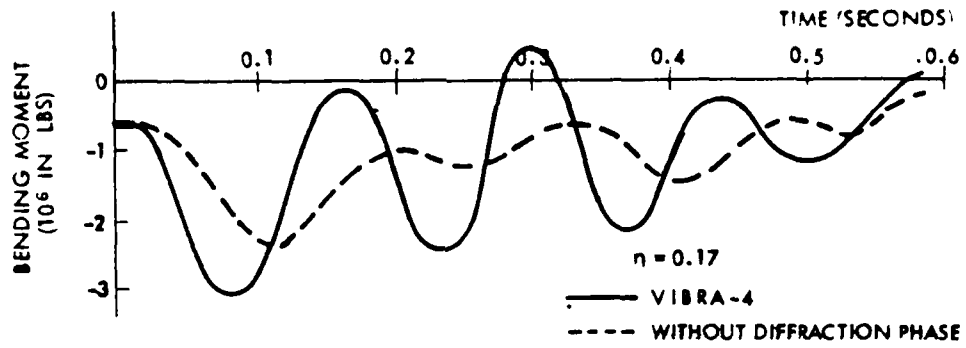


Figure 12 KC-135 right hand horizontal stabilizer - blast from above

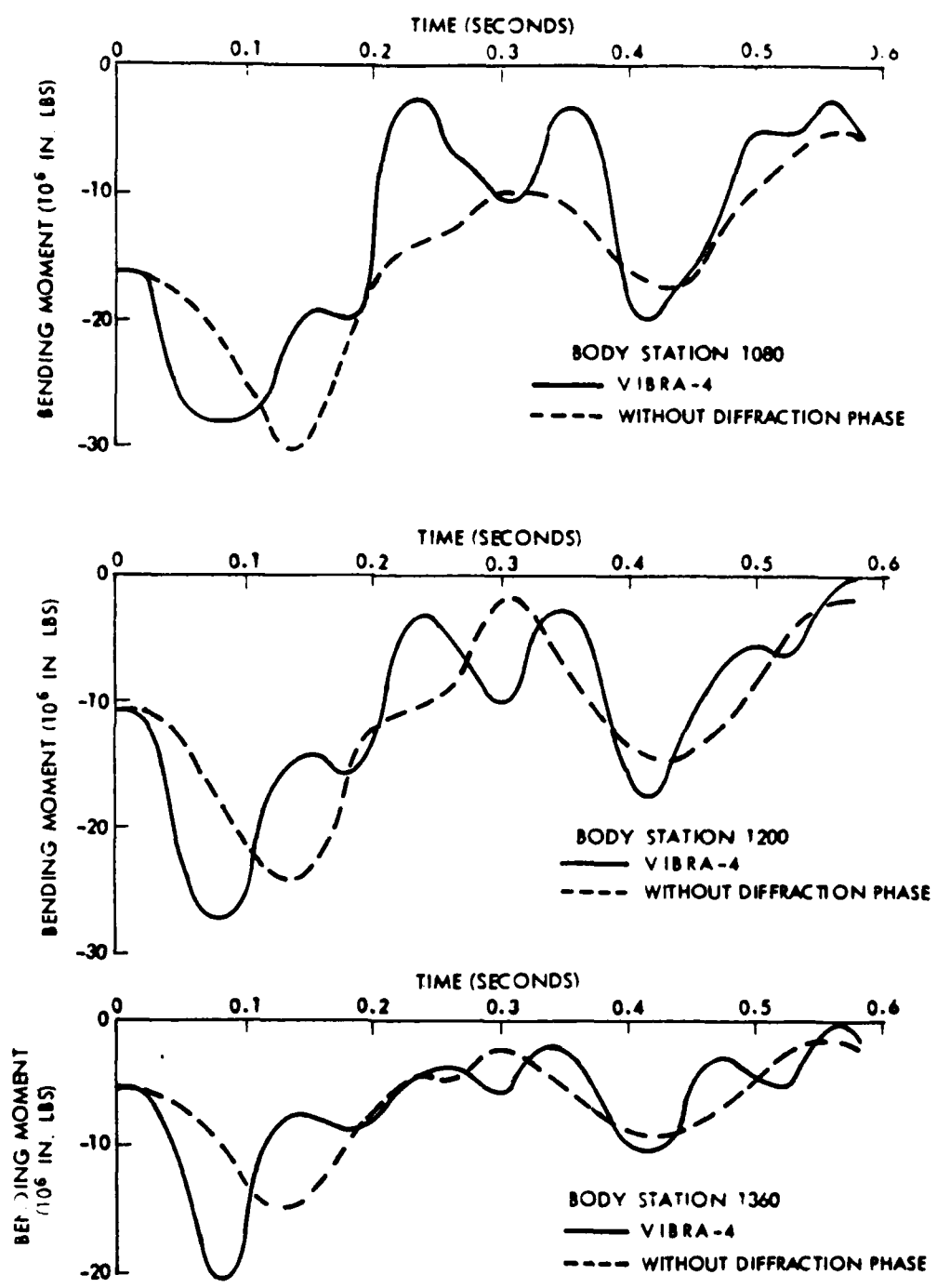


Figure 13 KC-135 body vertical bending - blast from above

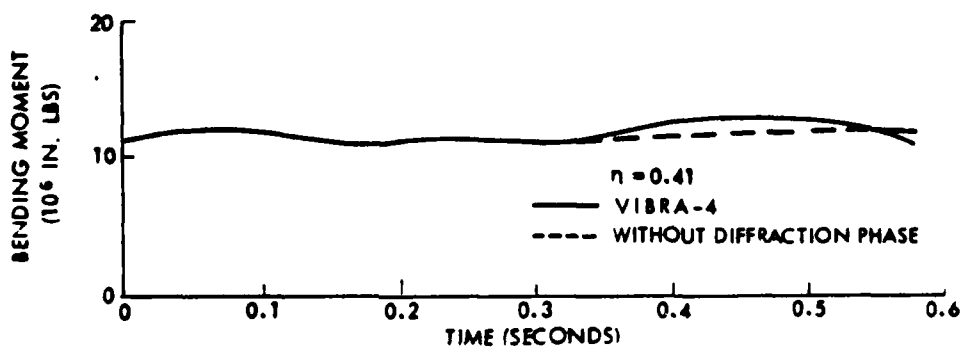
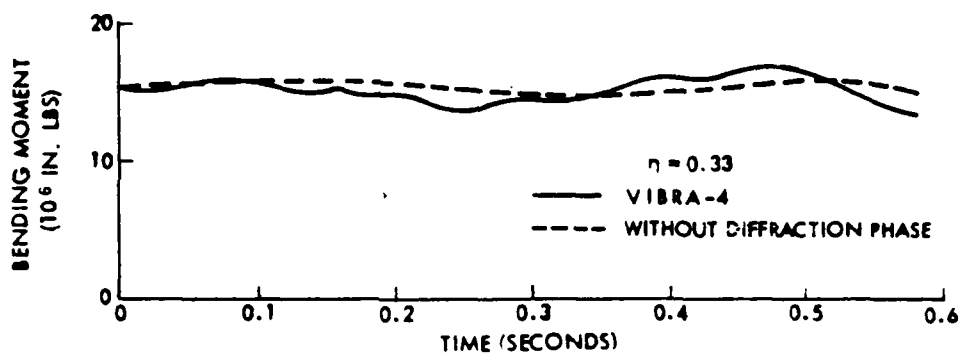
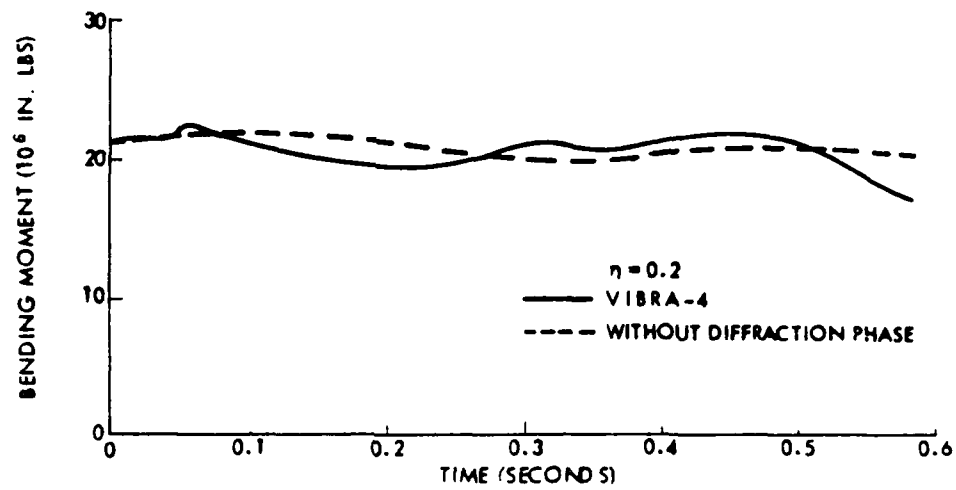


Figure 14 KC-135 right hand wing - blast from the side

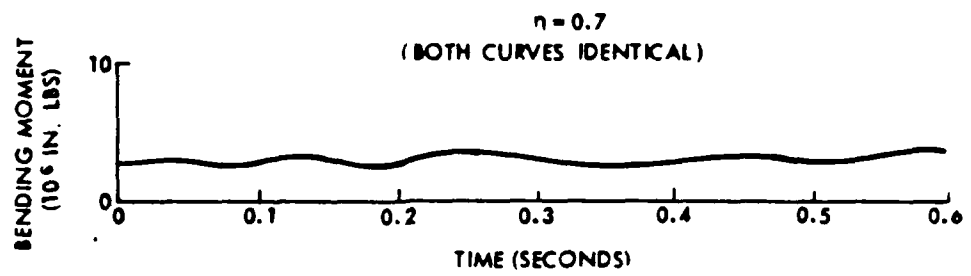
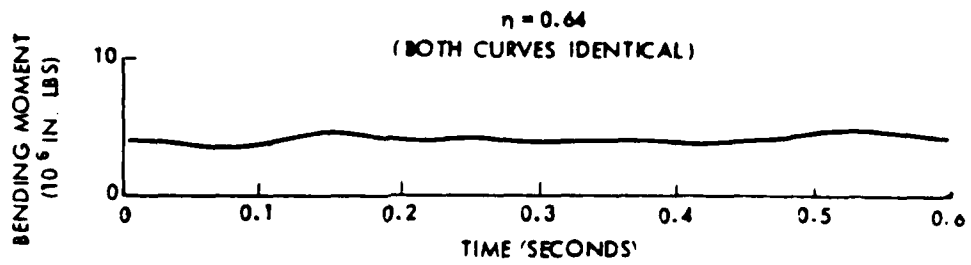


Figure 15 KC-135 right hand wing - blast from the side

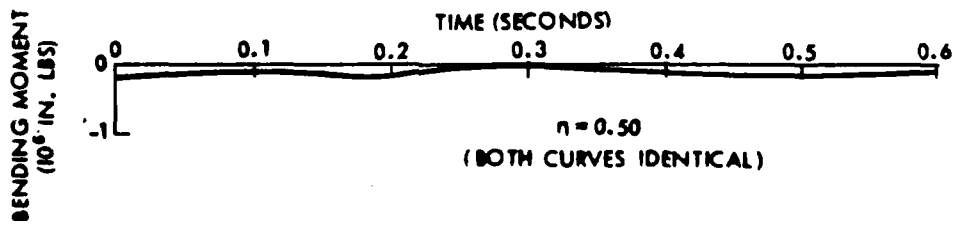
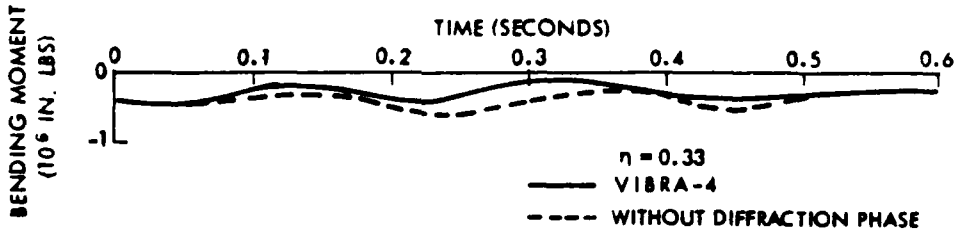
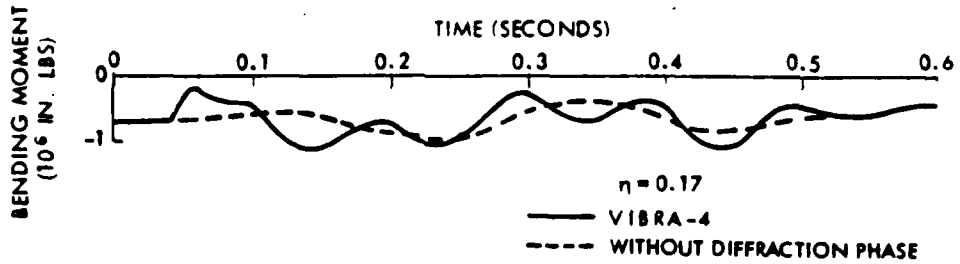


Figure 16 KC-135 left hand horizontal stabilizer - blast from the side

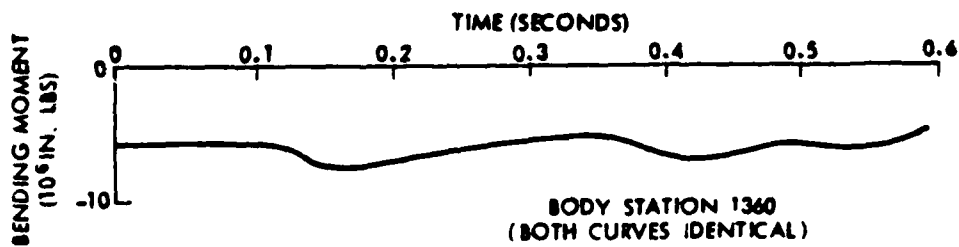
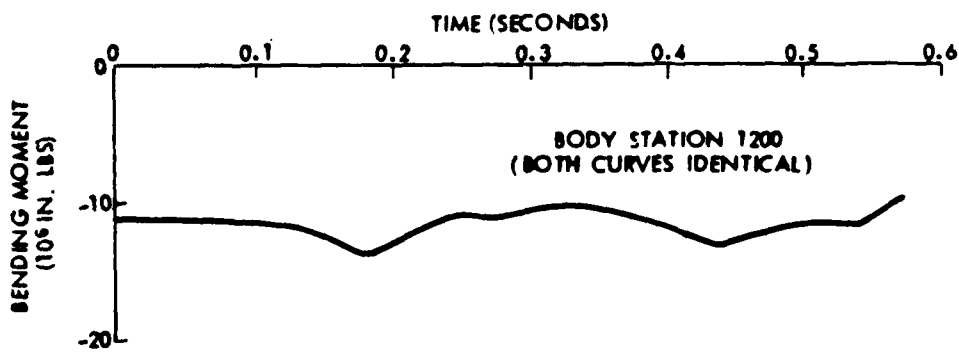
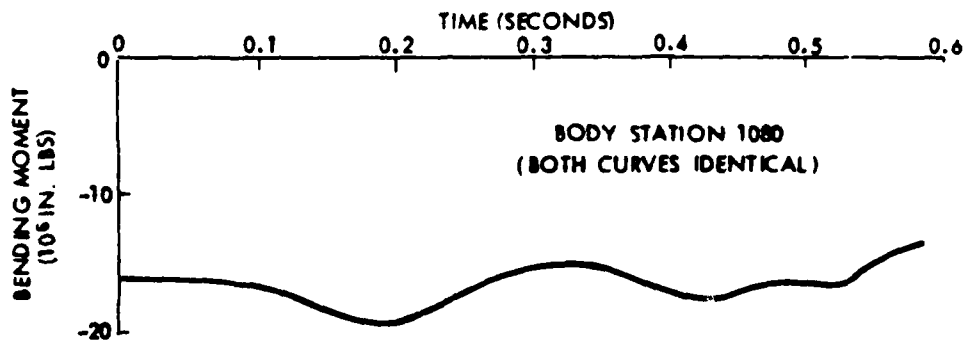


Figure 17 KC-135 vertical body bending - blast from the side

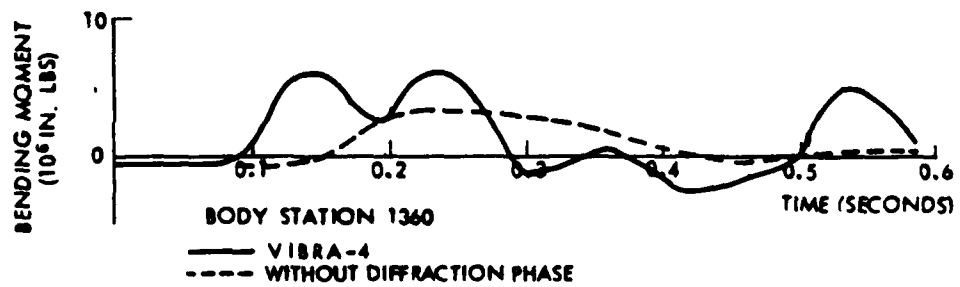
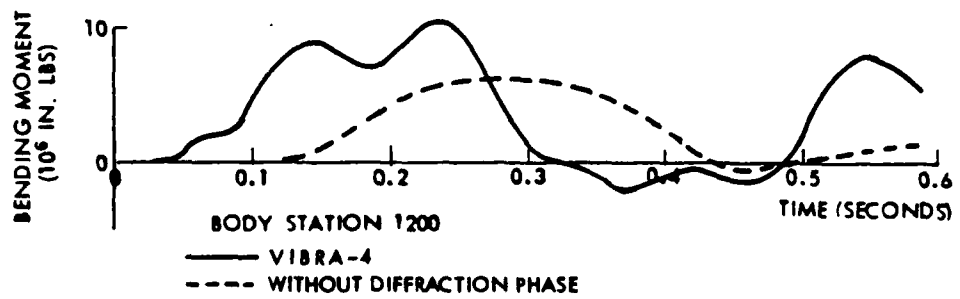
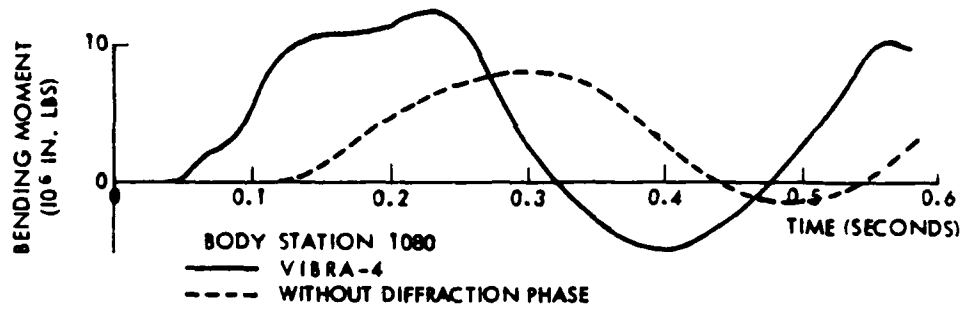


Figure 18 KC-135 horizontal body bending - blast from the side

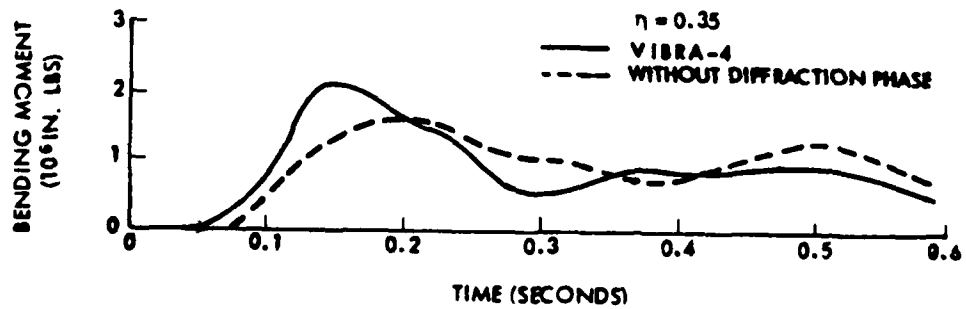
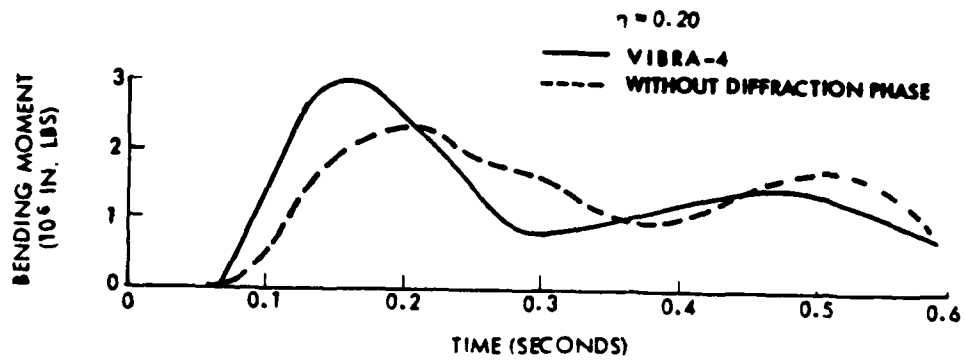


Figure 19 KC-135 fin - blast from the side

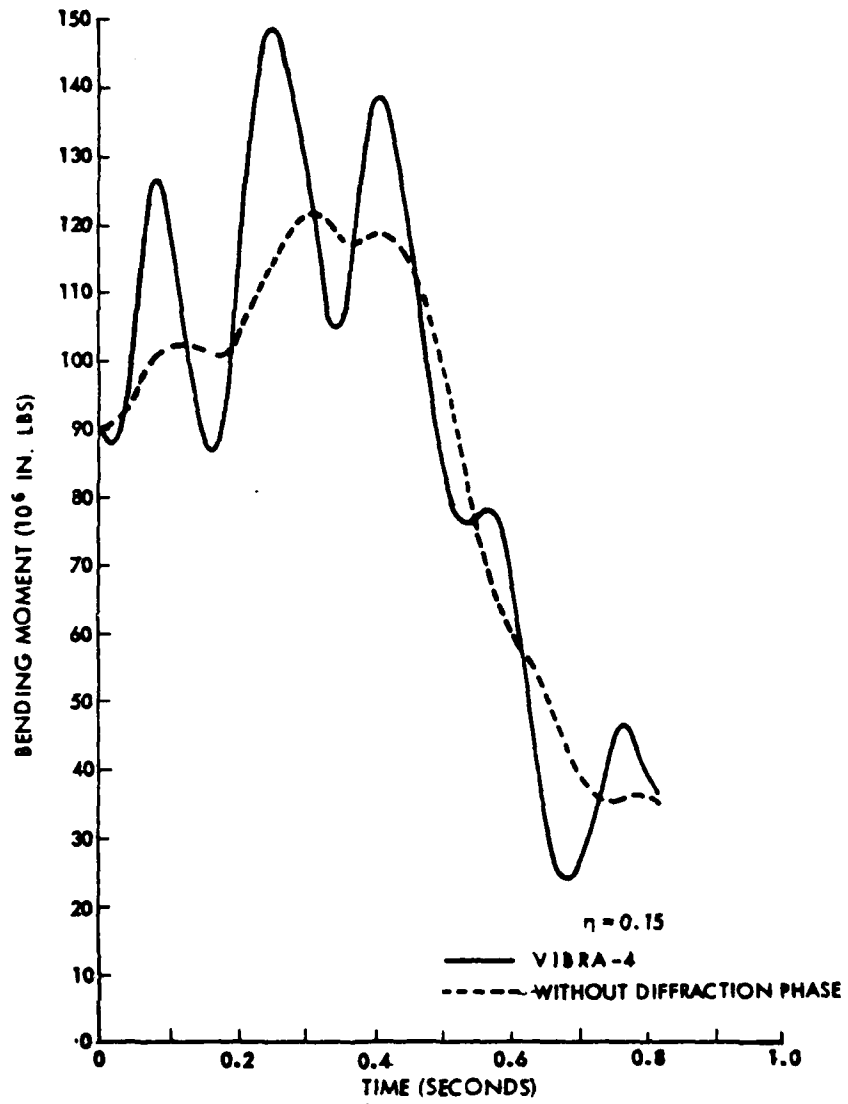


Figure 20. 747 right hand wing - blast from below

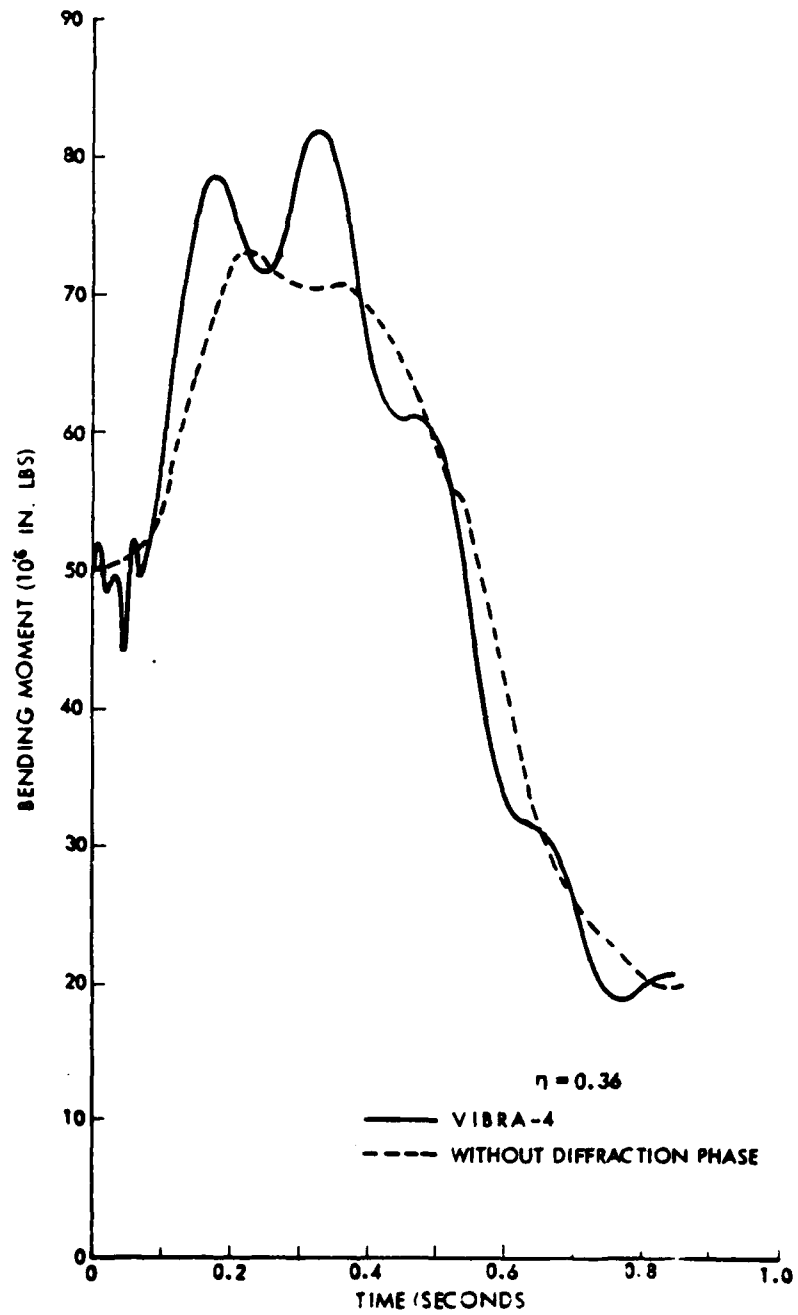


Figure 21 747 right hand wing - blast from below

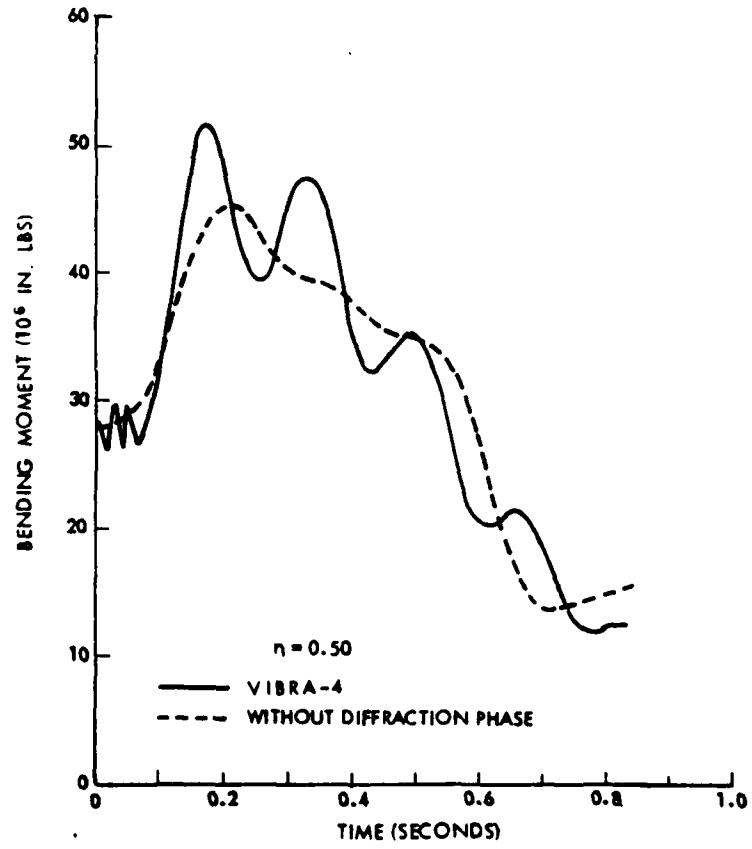


Figure 22 747 right hand wing - blast from below

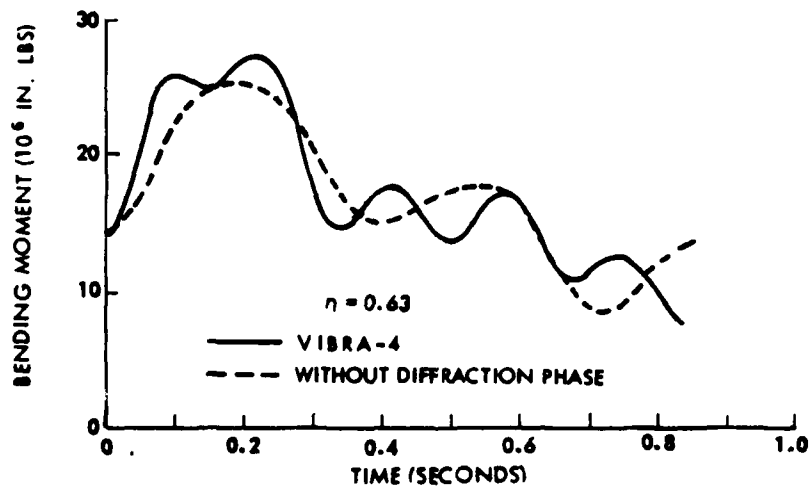
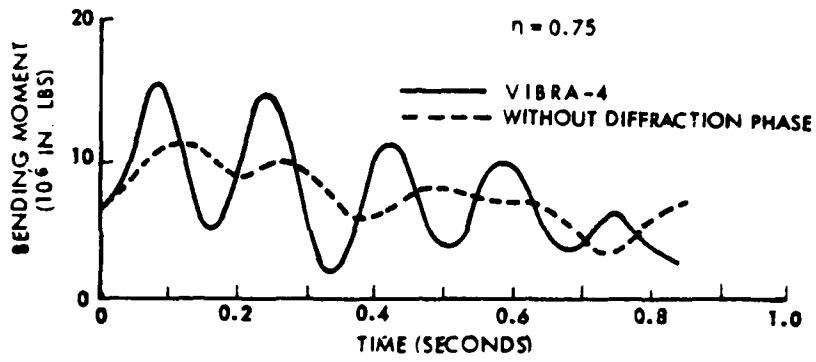


Figure 23 747 right hand wing - blast from below

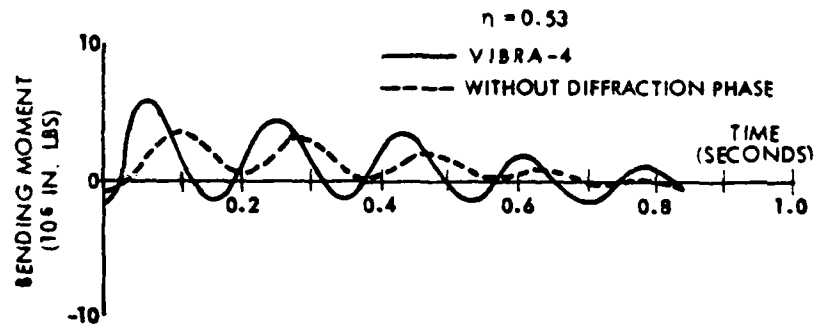
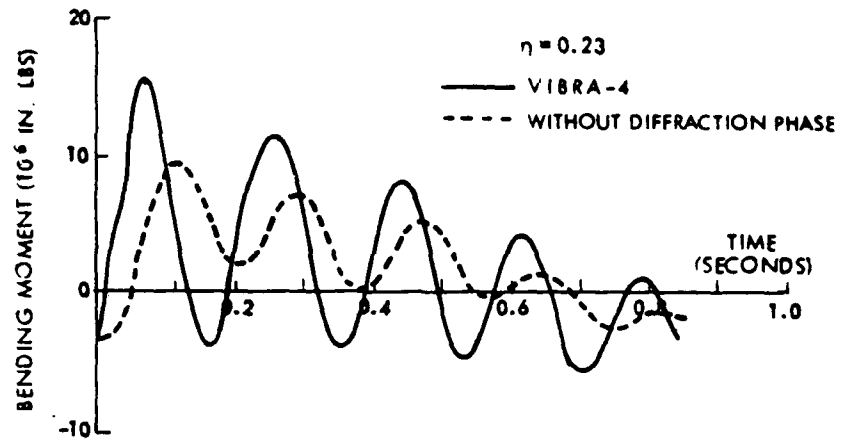


Figure 24 747 right hand horizontal stabilizer - blast from below

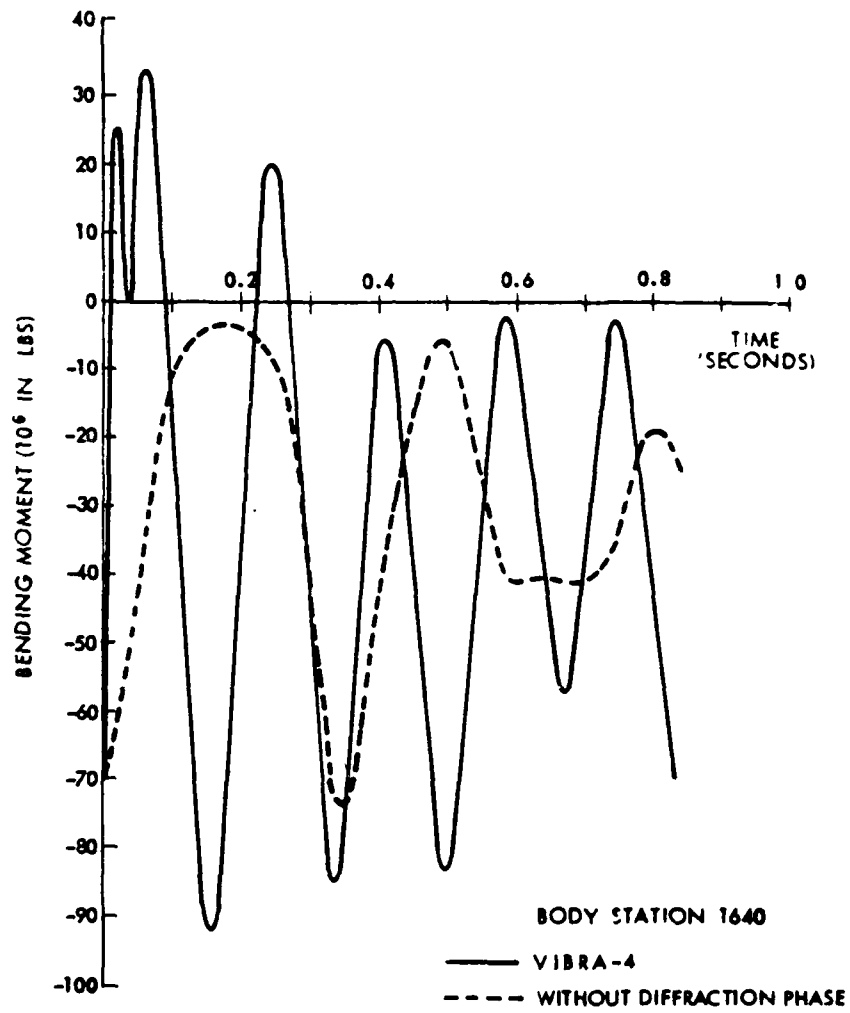


Figure 25 747 vertical body bending - blast from below

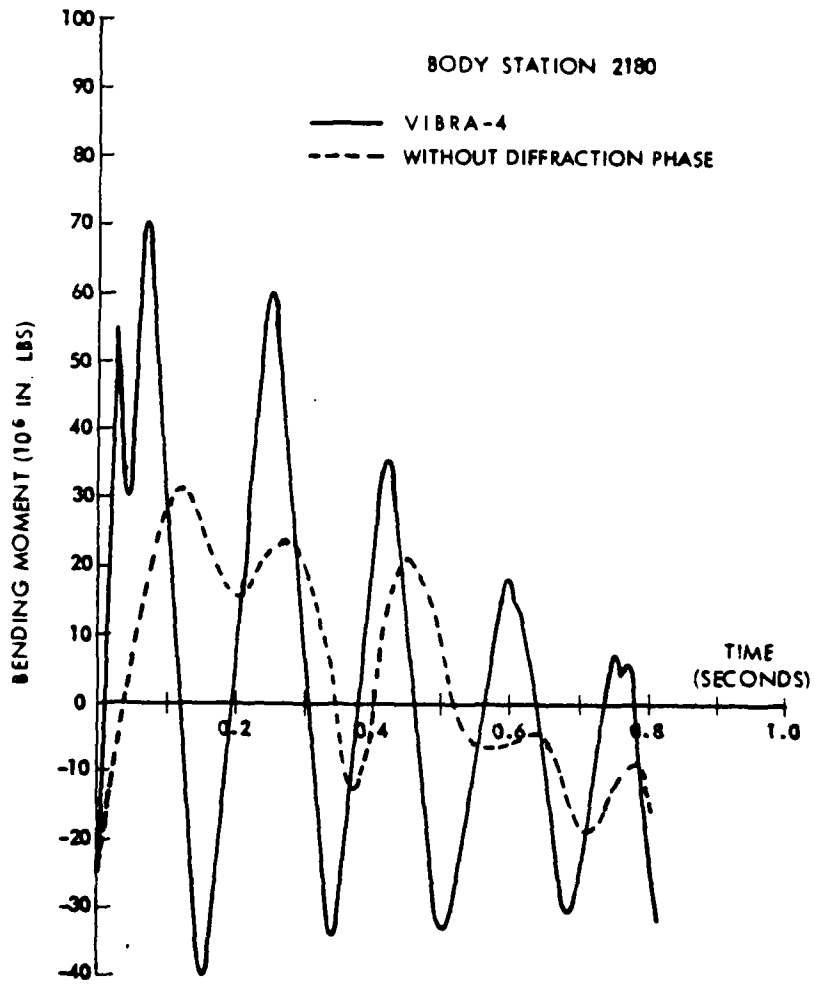


Figure 26 747 vertical body bending - blast from below

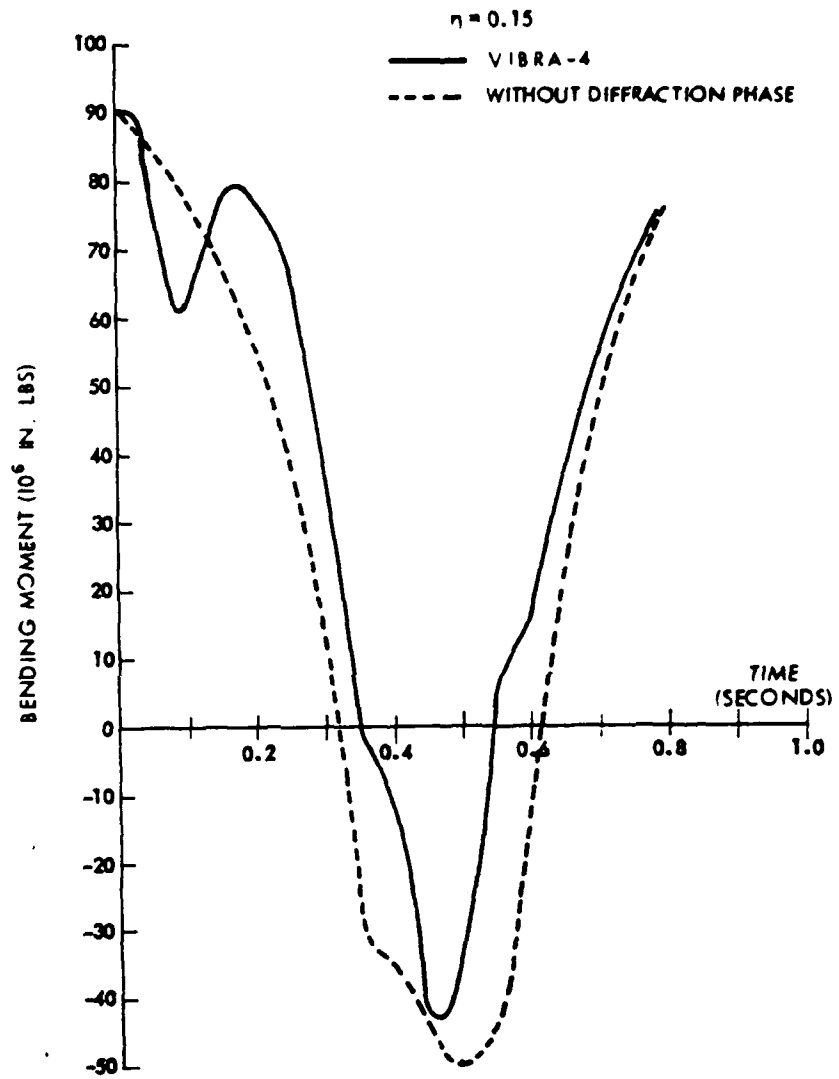


Figure 27 747 right hand wing - blast from above

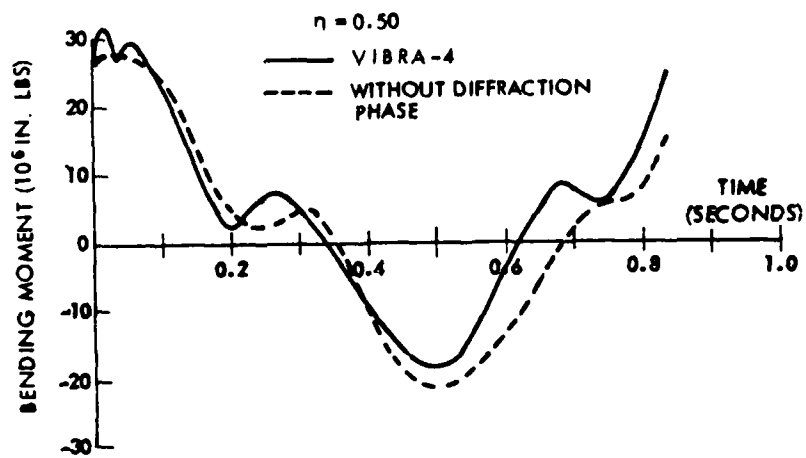
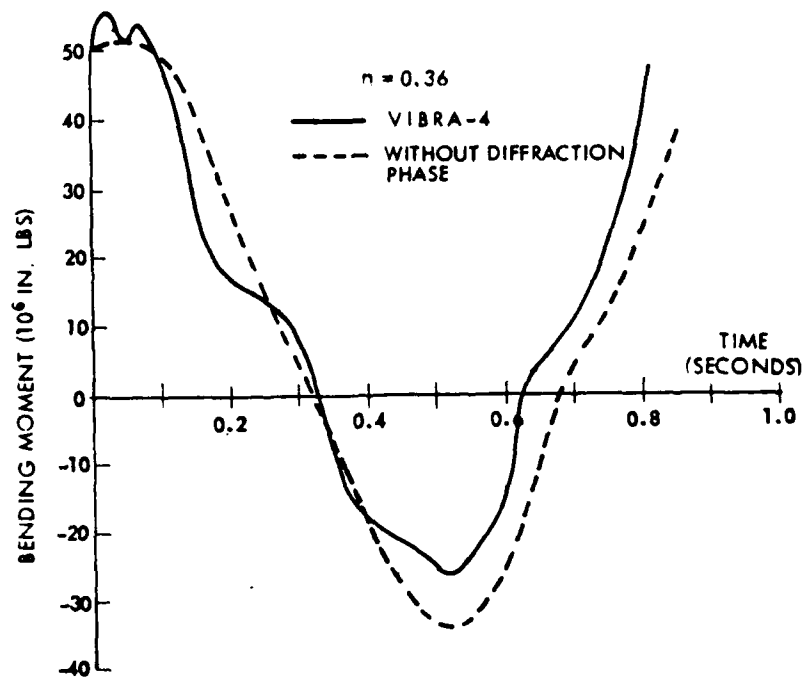


Figure 28 747 right hand wing - blast from above

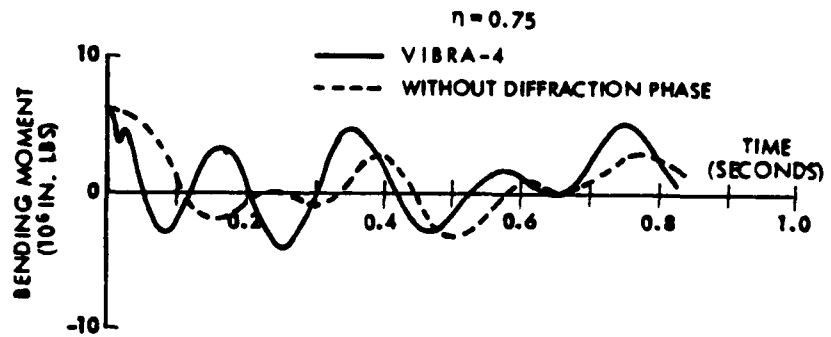
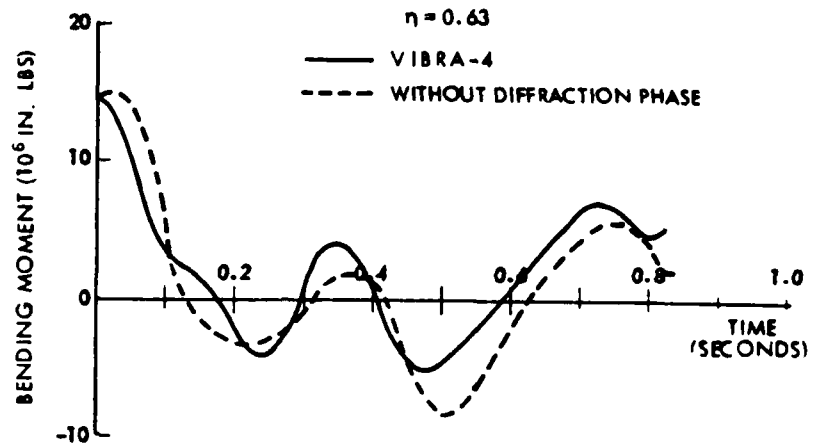


Figure 29 747 right hand wing - blast from above

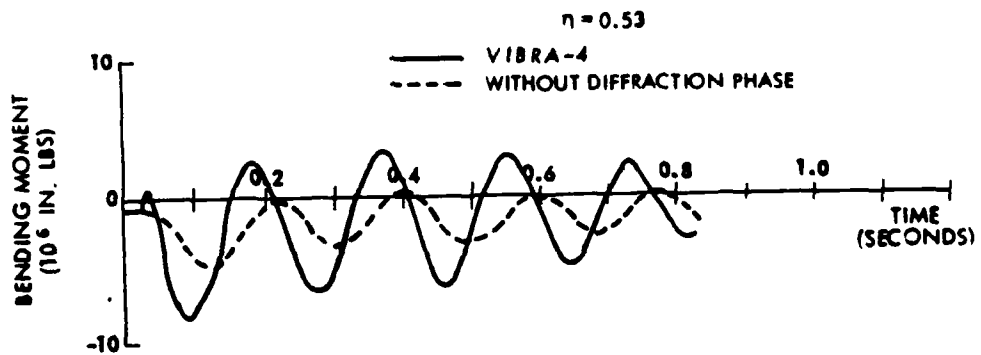
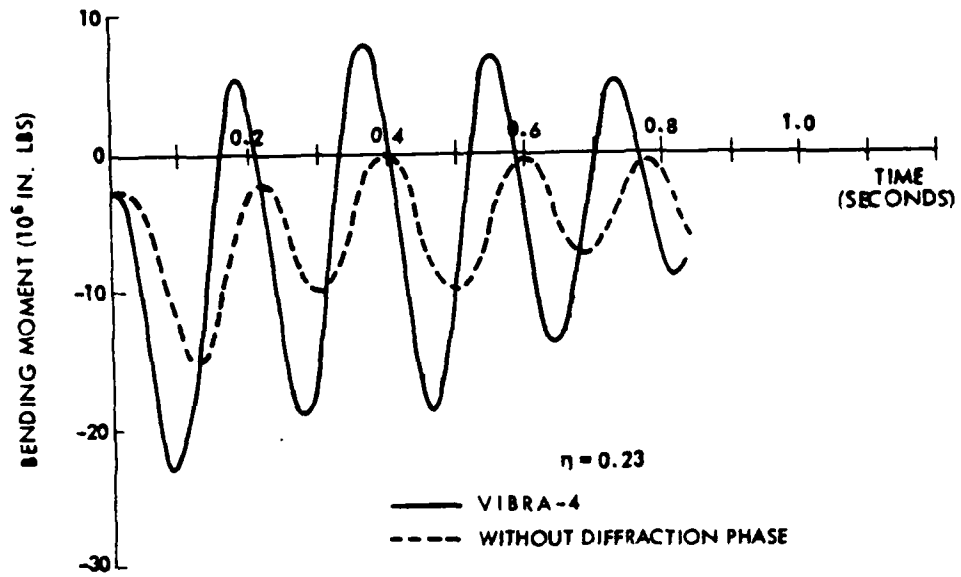


Figure 30 747 right hand horizontal stabilizer - blast from above

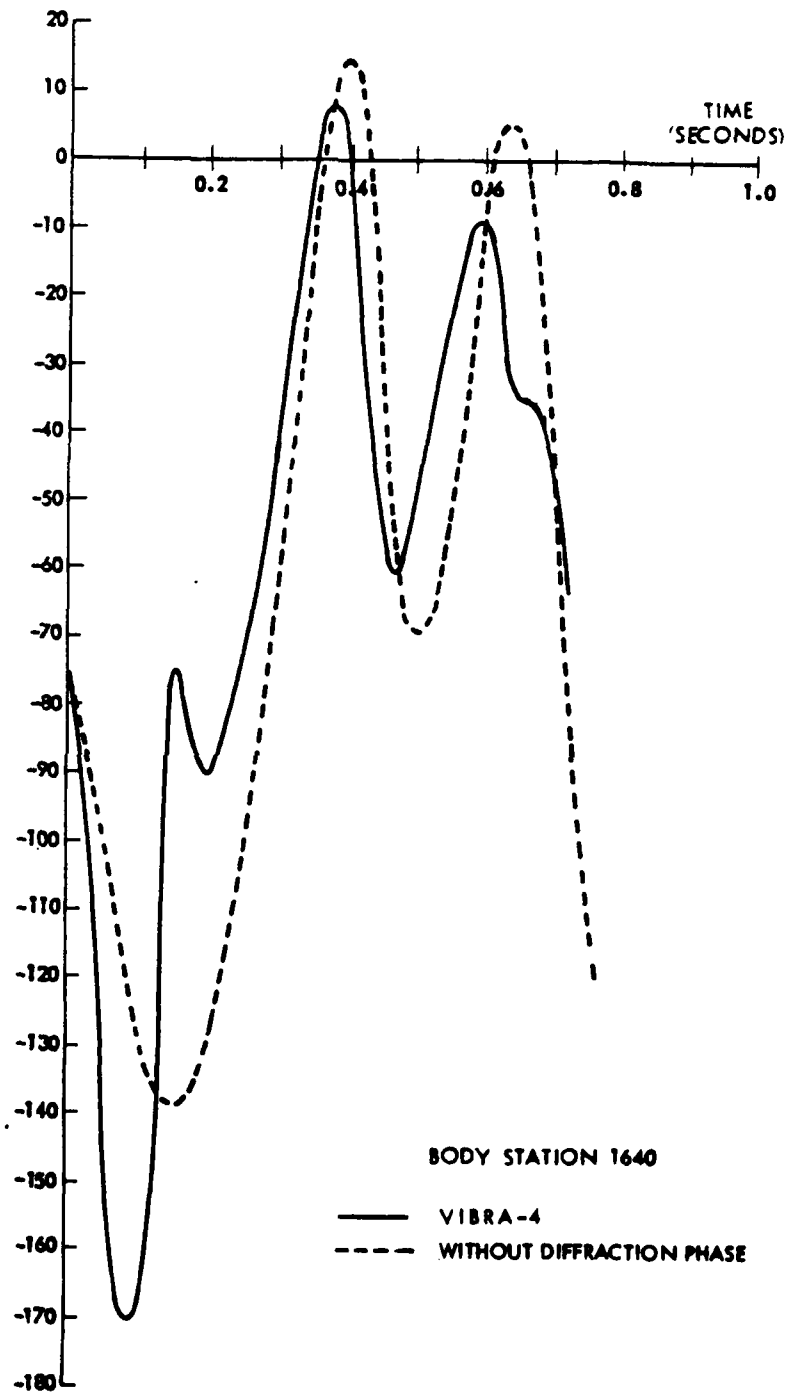


Figure 31 747 vertical body bending - blast from above

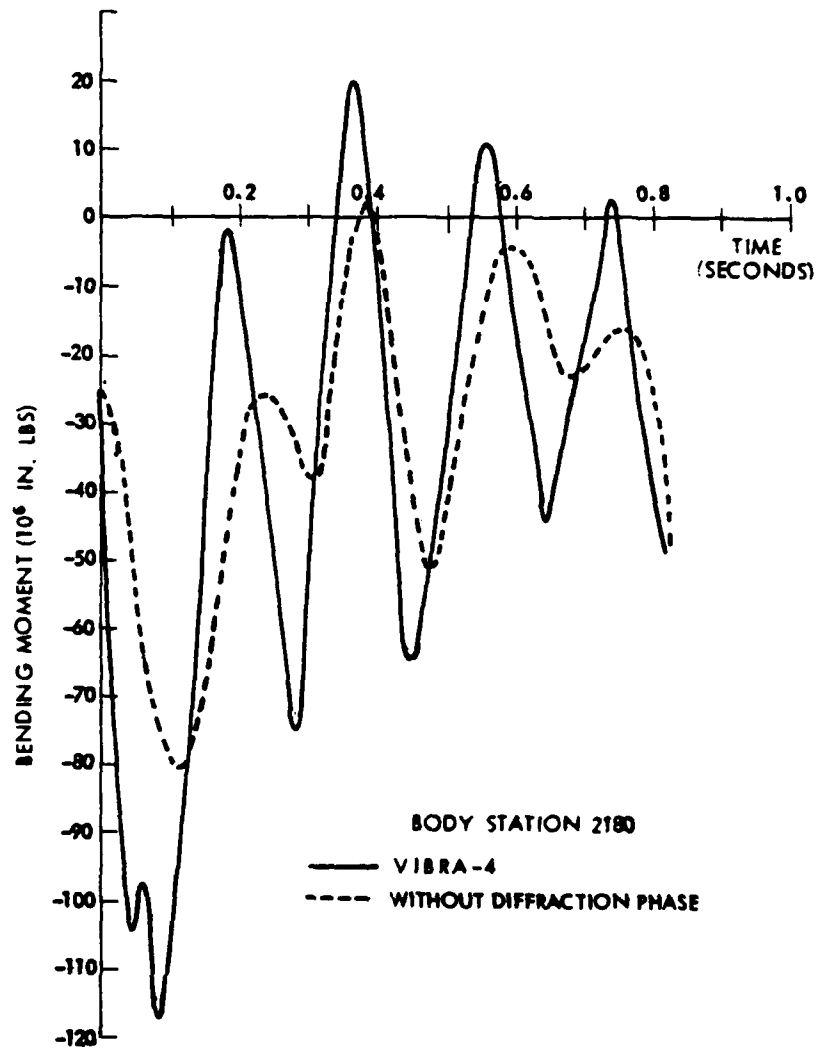


Figure 32 747 vertical body bending - blast from above

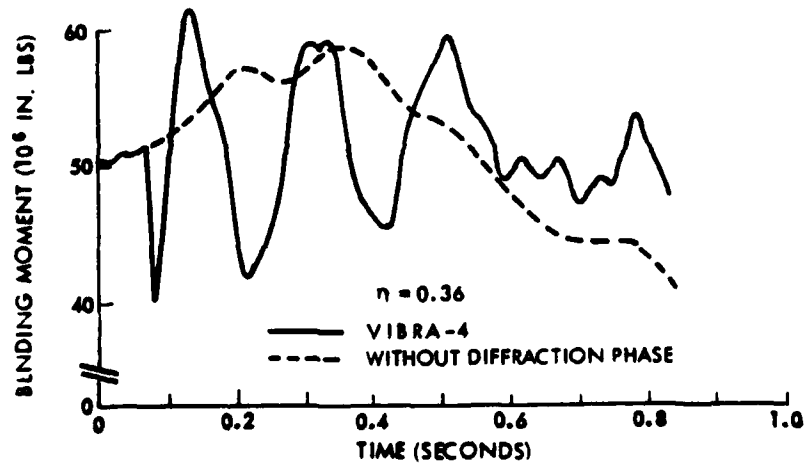
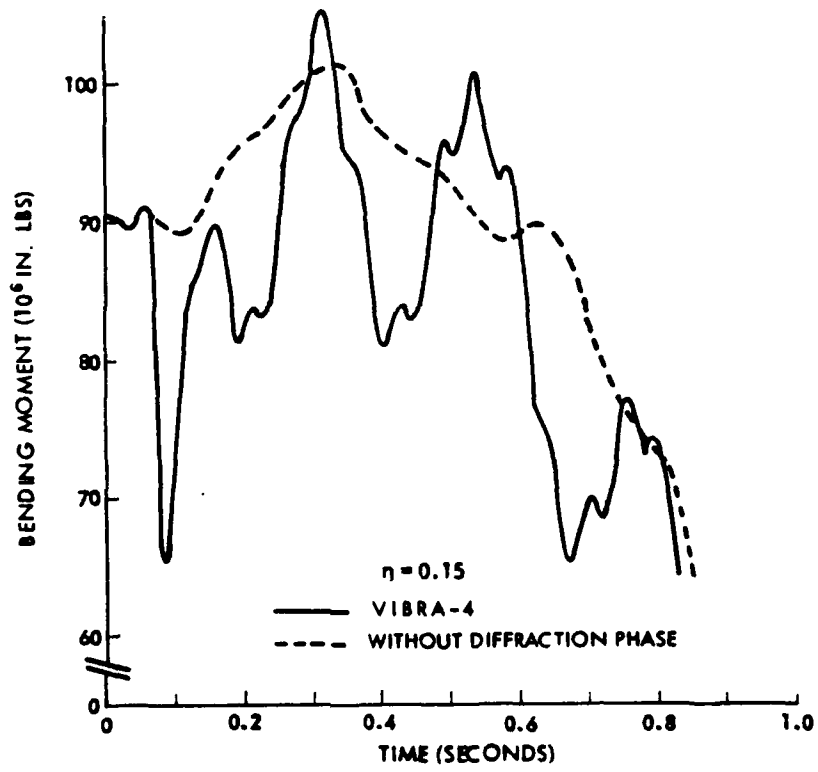


Figure 33 747 right hand wing - blast from side

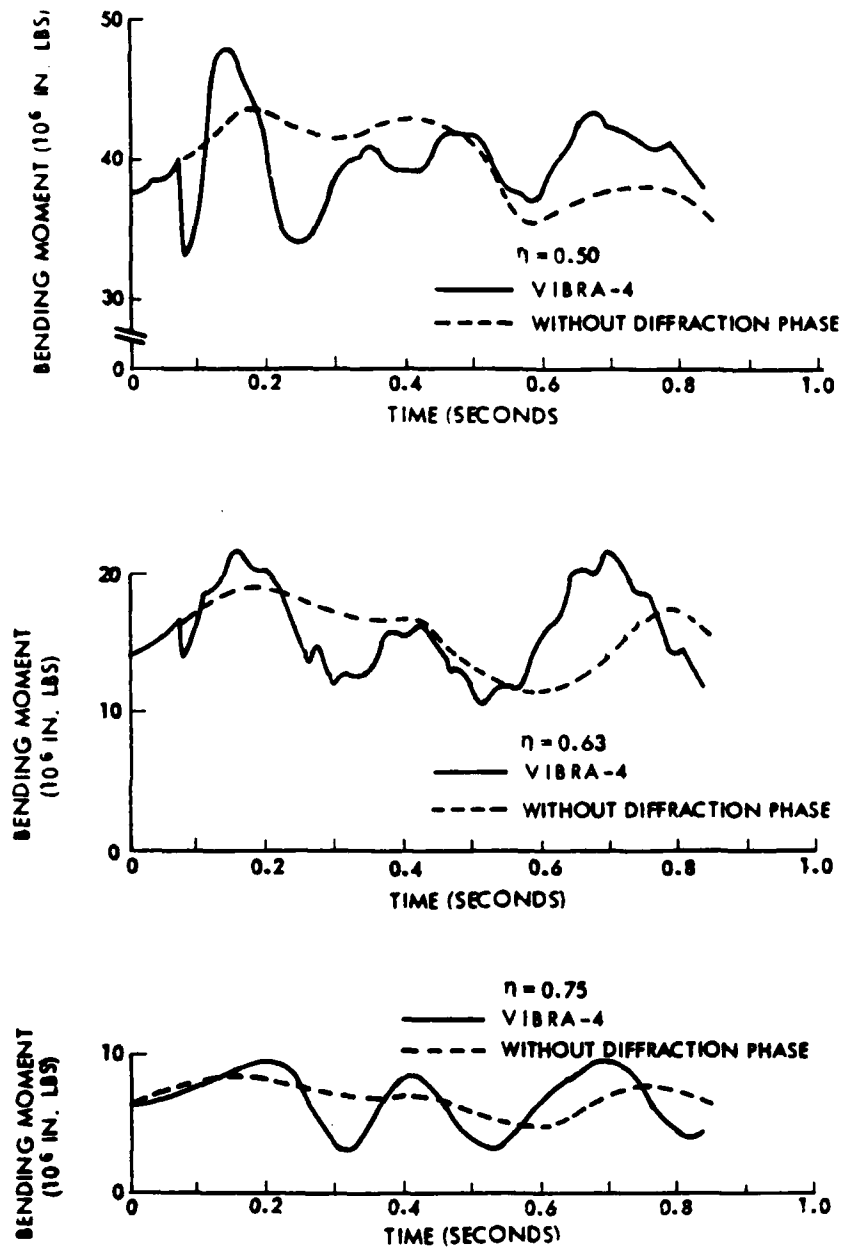


Figure 34 747 right hand wing - blast from side

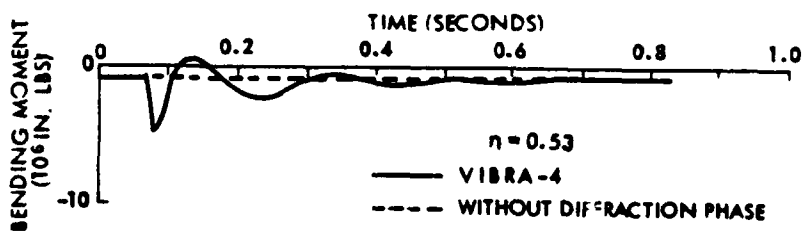
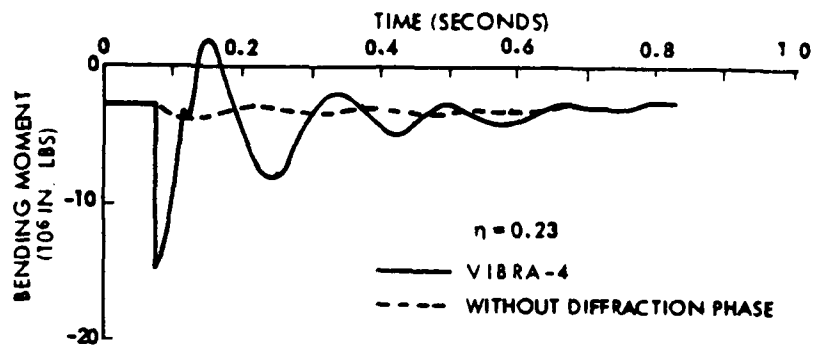


Figure 35 747 left hand horizontal stabilizer - blast from side

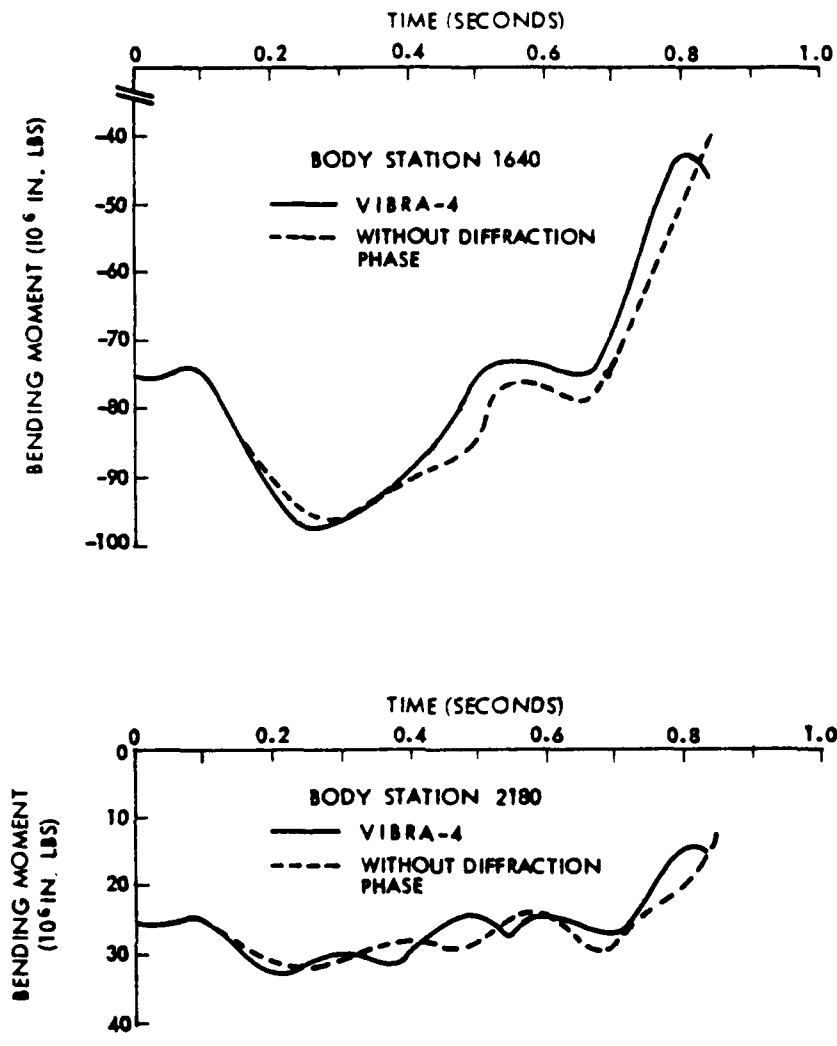


Figure 36 747 vertical body bending - blast from side

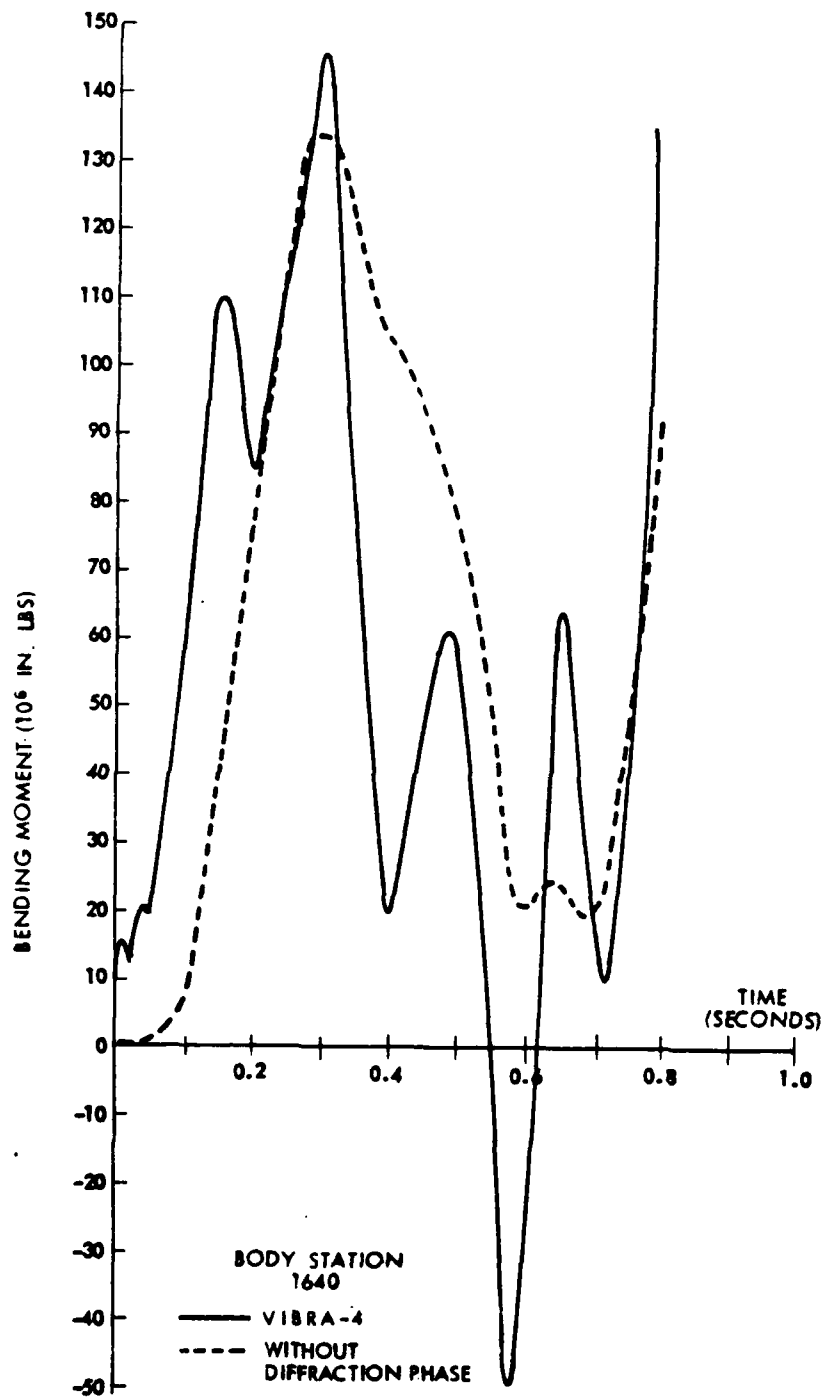


Figure 37 747 horizontal body bending - blast from side

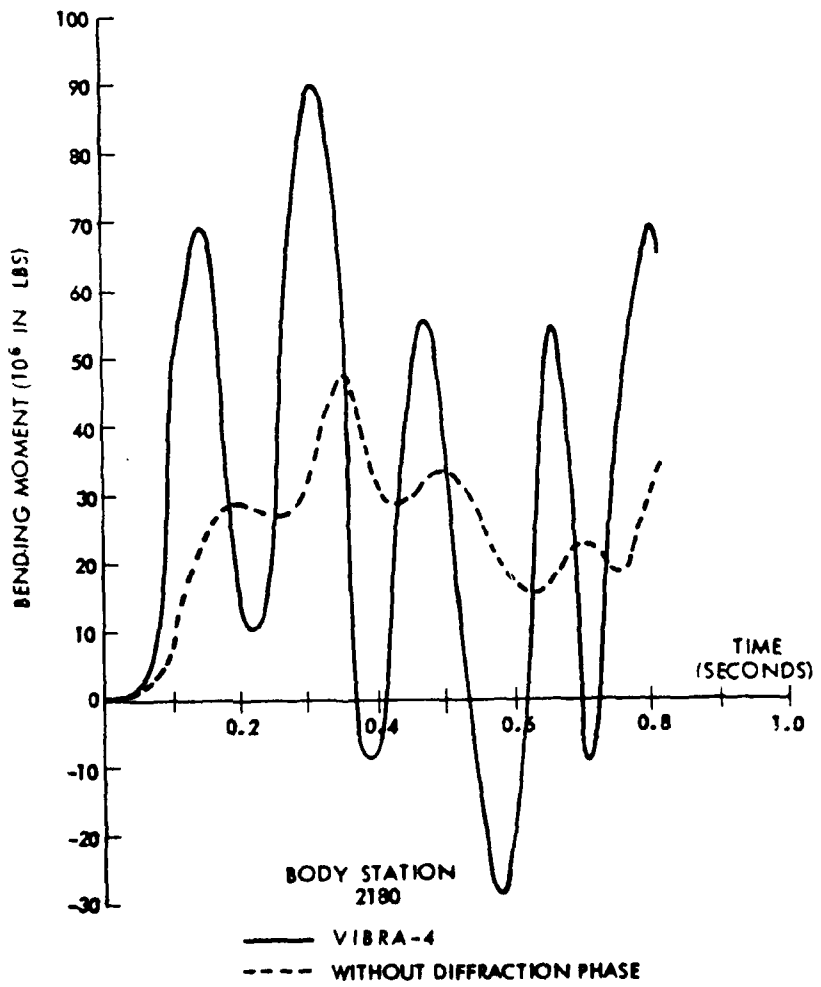


Figure 38 747 horizontal body bending - blast from side

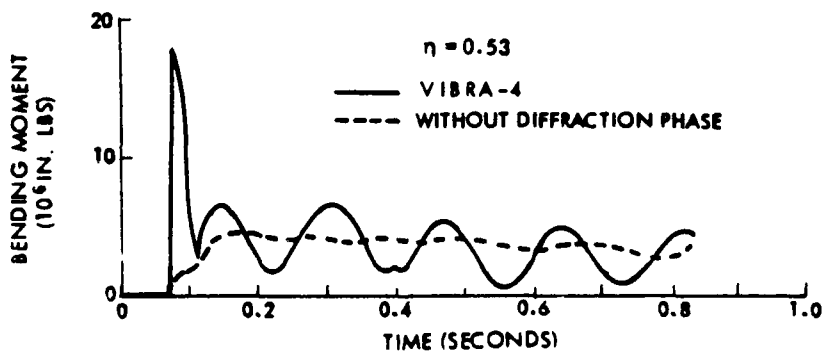
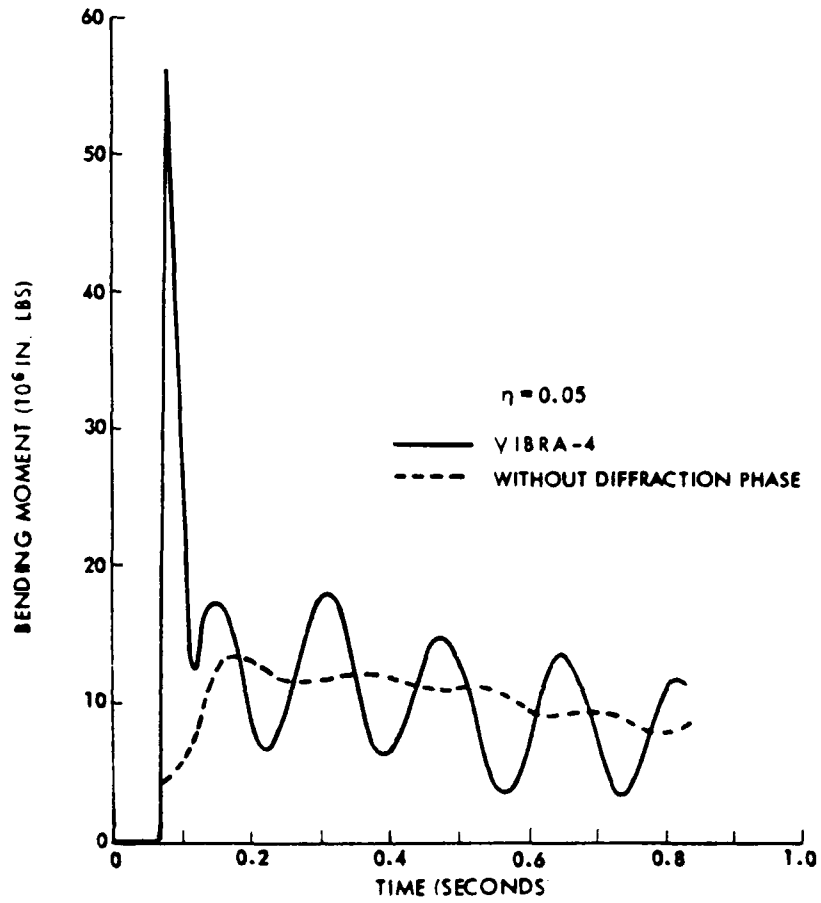


Figure 39 747 fin - blast from side

DISTRIBUTION LIST

DEPARTMENT OF DEFENSE

Assistant to the Secretary of Defense  
Atomic Energy  
ATTN: Executive Assistant

Defense Intelligence Agency  
ATTN: DB-4C, V. Fratzke

Defense Nuclear Agency  
ATTN: SPAS  
ATTN: STSP  
4 cy ATTN: TITL

Defense Technical Information Center  
12 cy ATTN: DD

Field Command  
Defense Nuclear Agency  
ATTN: FCT, W. Tyler  
2 cy ATTN: FCPR

Field Command  
Defense Nuclear Agency  
Livermore Division  
ATTN: FCPRL

NATO School (SHAPE)  
ATTN: U.S. Documents Officer

Undersecretary of Defense for Rsch. & Engrg.  
ATTN: Strategic & Space Systems (OS)

DEPARTMENT OF THE ARMY

Harry Diamond Laboratories  
Department of the Army  
ATTN: DELHD-N-P  
ATTN: DELHD-N-P, J. Gwaltney

U.S. Army Ballistic Research Labs.  
ATTN: DRDAR-BLT, W. Taylor

U.S. Army Materiel Dev. & Readiness Cmd.  
ATTN: DRCDE-D, L. Flynn

U.S. Army Nuclear & Chemical Agency  
ATTN: Library

DEPARTMENT OF THE NAVY

Naval Material Command  
ATTN: MAT 08T-22

Naval Research Laboratory  
ATTN: Code 2627

Naval Surface Weapons Center  
ATTN: Code F31, K. Caudle

Naval Weapons Evaluation Facility  
ATTN: L. Oliver

Office of Naval Research  
ATTN: Code 465

DEPARTMENT OF THE NAVY (Continued)

Strategic Systems Project Office  
Department of the Navy  
ATTN: NSP-272

DEPARTMENT OF THE AIR FORCE

Aeronautical Systems Division  
Air Force Systems Command  
ATTN: ASD/ENFT, R. Bachman  
4 cy ATTN: ASD/ENFTV, D. Ward

Air Force Aero-Propulsion Laboratory  
ATTN: TBC, M. Stibich

Air Force Materials Laboratory  
ATTN: MBE, G. Schmitt

Air Force Weapons Laboratory  
Air Force Systems Command  
ATTN: DYV, A. Sharp  
ATTN: SUL  
ATTN: DYV, G. Campbell

Assistant Chief of Staff  
Studies & Analyses  
Department of the Air Force  
ATTN: AF/SASC, B. Adams  
ATTN: AF/SASB, R. Mathis

Deputy Chief of Staff  
Research, Development, & Acq.  
Department of the Air Force  
ATTN: AFRDP, N. Alexandrow

Foreign Technology Division  
Air Force Systems Command  
ATTN: SDBF, S. Spring

Strategic Air Command  
Department of the Air Force  
ATTN: XPFS, B. Stephan  
ATTN: XPFS, F. Tedesco

DEPARTMENT OF ENERGY CONTRACTOR

Sandia Laboratories  
ATTN: A. Lieber

DEPARTMENT OF DEFENSE CONTRACTORS

AVCO Research & Systems Group  
ATTN: J. Patrick  
ATTN: P. Grady

BDM Corp.  
ATTN: C. Somers

Boeing Co.  
ATTN: S. Strack  
ATTN: M/S 85/20, E. York  
ATTN: R. Dyrdaht

DEPARTMENT OF DEFENSE CONTRACTORS (Continued)

Boeing Wichita Co.  
ATTN: R. Syring  
ATTN: K. Rogers

Calspan Corp.  
ATTN: M. Dunn

University of Dayton  
ATTN: B. Wilt

Effects Technology, Inc.  
ATTN: R. Wengler  
ATTN: R. Globus  
ATTN: R. Parisse  
ATTN: E. Bick

General Electric Company—TEMPO  
ATTN: DASIAC

General Research Corp.  
ATTN: T. Stathacopoulos

Kaman Avidyne  
ATTN: B. Lee  
ATTN: R. Ruetenik  
ATTN: E. Criscione  
ATTN: N. Hobbs

DEPARTMENT OF DEFENSE CONTRACTORS (Continued)

Kaman Sciences Corp.  
ATTN: D. Sachs

Los Alamos Technical Associates, Inc.  
ATTN: P. Hughes  
ATTN: C. Sparling

McDonnell Douglas Corp.  
ATTN: J. McGrew

Prototype Development Associates, Inc.  
ATTN: C. Thacker  
ATTN: J. McDonald  
ATTN: H. Moody

R & D Associates  
ATTN: J. Carpenter  
ATTN: F. Field  
ATTN: A. Kuhl  
ATTN: C. MacDonald

Rockwell International Corp.  
ATTN: R. Moonan

Science Applications, Inc.  
ATTN: J. Dishon

END

DATE  
FILMED

8-80

DTIC